

available at www.sciencedirect.comjournal homepage: www.elsevier.com/locate/jmbbm

Research paper

Dimensional analysis and parametric studies for designing artificial nacre

Jee E. Rim^a, Pablo Zavattieri^b, Allison Juster^a, Horacio D. Espinosa^{a,*}

^a Department of Mechanical Engineering, Northwestern University, Evanston, IL 60208-3111, USA

^b School of Civil Engineering, Purdue University, West Lafayette, IN 47907-2051, USA

ARTICLE INFO

Article history:

Received 26 July 2010

Received in revised form

10 November 2010

Accepted 11 November 2010

Published online 24 November 2010

Keywords:

Nacre

Biomimetics

Dimensional analysis

Size effects

Rapid prototyping

Multiscale modeling

Nanocomposites

ABSTRACT

Nacre, the iridescent material found in Abalone shells, exhibits remarkable strength and toughness despite its composition of over 95% brittle ceramic. Its hierarchical structure over multiple length scales gives rise to its increase in toughness despite its material composition. In this work we develop a computational model of composites incorporating key morphological features of nacre's microstructure. By conducting a parametric analysis we are able to determine an optimal geometry that increases energy dissipation over 70 times. We discuss the contribution of varying ceramic strengths and size effect to see how this affects the overall performance of the composite. We then compare our simulations to experiments performed on a material possessing the same microstructure investigated computationally. For both simulations and experiments we show that our optimal geometry corresponds to that of natural nacre indicating the importance of specifically incorporating nacre's key morphological and constituent features. This combination of simulations and experiments gives great insight to the delicate interplay between material parameters and microstructure showing that if we optimally combine all aspects, we can develop novel synthetic materials with superior performance.

© 2010 Elsevier Ltd. All rights reserved.

1. Introduction

Natural materials can exhibit remarkable combinations of stiffness, low weight, strength and toughness, which are in some cases unmatched by manmade materials. In the past two decades significant efforts were undertaken in the materials research community to elucidate the microstructure and mechanisms behind these mechanical performances, with the goal of duplicating them in artificial materials (Barthelat et al., 2009; Mayer, 2005, 2006; Sarikaya and Aksay, 1995). This approach to design, called biomimetics, has now started

to yield materials with remarkable properties. The first step in this biomimetic approach is the identification of material performance in natural materials, together with a fundamental understanding of the mechanisms behind these performances.

Nacre is an excellent example of such a high-performance natural material. It is composed of at least 95% calcium carbonate in aragonite form, yet by comparison with the brittle ceramic, nacre exhibits a 1000-fold increase in toughness at the expense of a small reduction in stiffness. This is achieved through a complex hierarchical structure

* Corresponding author. Tel.: +1 847 4675989; fax: +1 847 4913915.

E-mail address: espinosa@northwestern.edu (H.D. Espinosa).

Nomenclature

θ	Dovetail angle
L	Half tablet length
L_o	Length of overlap between tablets
t	Tablet thickness
b	Bridge thickness
h	Thickness of filler
E^T	Modulus of tablet
E^F	Modulus of filler
σ_y^F	Filler yield stress
σ_f^T	Strength of tablet
ν^T	Poisson's ratio tablet
ν^F	Poisson's ratio of filler
K	Initial stiffness of composite
T_{\max}	Maximum traction
J	Fracture energy
μ	Friction coefficient between filler and tablet
σ_1^T	Maximum principal stress in composite
σ_f^C	Maximum stress up to failure of composite
U^C	Strain energy absorbed by composite
E^F/E^T	Material dimensionless group
σ_f^T/E^T	Material dimensionless group
σ_y^F/E^T	Material dimensionless group
KL/E^T	Material dimensionless group
T_{\max}/σ_f^T	Relative maximum traction
$E^F J/T_{\max}^2 L$	Relative fracture length scale
L_o/L	Geometric dimensionless group
t/L	Geometric dimensionless group
b/L	Geometric dimensionless group
h/L	Geometric dimensionless group
σ_f^R	Reference stress at yield of composite with 0° dovetail sample
U^R	Strain energy absorbed at yield of 0° dovetail sample
σ_f^C/σ_f^R	Relative stress of composite
U^C/U^R	Relative energy absorbed by composite

organized over several length scales, with mechanisms operating at the nanoscale and above (Ballarini et al., 2005; Barthelat et al., 2009; Espinosa et al., 2009; Gao et al., 2003). The combination of strength and toughness of nacre has inspired a large class of biomimetic materials and organic/inorganic composites (Ortiz and Boyce, 2008). The creation of an artificial shell material with its intricate microstructure is a challenge that requires both the design of optimum microstructures and the development of fabrication procedures to implement these designs (Bonderer et al., 2008; Chen et al., 2007a; Deville et al., 2006; He et al., 1997; Heuer et al., 1992; Kato, 2000; Podsiadlo et al., 2007a,b; Sellinger et al., 1998; Tang et al., 2003; Wei et al., 2007; Zhang et al., 2006). A variety of fabrication methods have been proposed and tested in the last decade, demonstrating the increase in strength and toughness of composites that utilize the deformation mechanisms of nacre; however, there is a lack of quantitative and comprehensive analysis of the design parameters that allow the mechanisms to operate.

The microscale architecture of nacre resembles a three-dimensional brick and mortar structure, where the bricks are densely packed layers of microscopic aragonite polygonal tablets (about 5–8 μm in diameter and about 0.5 μm in thickness) held together by 20–30 nm thick layers of organic materials (Fig. 1(b)–(d)). While the tablets are generally described and modeled as flat at the microscale (Evans et al., 2001; Kotha et al., 2001), they actually exhibit a significant waviness (Barthelat et al., 2007). This feature has been observed with optical microscopy, scanning probe microscopy, scanning and transmission electron microscopy (Fig. 1(e)). The roughness can reach amplitudes of 200 nm, which is a significant fraction of the tablet's thickness of about 500 nm (Barthelat et al., 2007).

It is widely recognized that tablet sliding is a key mechanism in the toughness of nacre (Barthelat et al., 2007; Jackson et al., 1988; Kotha et al., 2001; Wang et al., 2001). It was recently proposed that the hardening mechanism is generated by the waviness of the surfaces (Barthelat et al., 2007). As the layers slide on one another, the tablets must climb each others' waviness, which generates progressive tablet interlocking and an increasing resistance to sliding. In addition, such mechanisms could generate the observed transverse expansion, while the organic glue and mineral bridges maintain cohesive strength between tablets. Fig. 2(a) shows an actual image of the structure of nacre. Tablet waviness is evident, and it can be seen that it generates dovetail-like features at the end of some tablets. Such structure, loaded in tension, will generate progressive locking, hardening and spreading of non-linear deformation around cracks and defects at large scales (Fig. 2(b)). Microstructure based three dimensional finite element models have also demonstrated that waviness was indeed a key feature to generate hardening in nacre (Barthelat et al., 2007; Tang et al., 2007). The associated viscoplastic energy dissipation at the interfaces between tablets greatly enhances the toughness of nacre, arresting cracks before they become a serious threat to the shell and to the life of the animal (Barthelat and Espinosa, 2007; Wang et al., 2001).

Nacre exhibits structural features down to the nanoscale, at the 20–30 nm interfaces between the tablets. The organic material that fills this space and bonds the tablets together is composed of several layers of various proteins and chitin (Schaeffer et al., 1997; Smith et al., 1999). These sheets of organic layers contain pores with a 20–100 nm spacing, leaving space for two types of aragonite structures: nanoasperities and direct aragonite connections across the interfaces (mineral “bridges” connecting tablets). The height and width of these features vary from 10 to 30 nm while their spacing is in the order of 100–200 nm (Barthelat et al., 2006).

A number of striking and relevant features are revealed in uniaxial tension (Barthelat et al., 2007), along the direction of the tablets, and in crack propagation experiments (Barthelat and Espinosa, 2007; Espinosa et al., 2009). Fig. 3(a) shows the tensile behavior of nacre, showing some ductility at the macroscale. The stress–strain curve shows relatively large deformations, accompanied by hardening up to failure at a microscopic strain of almost 1%. Full strain field measurements revealed local strain values of 2% (Barthelat and Espinosa, 2007), as well as significant expansion across

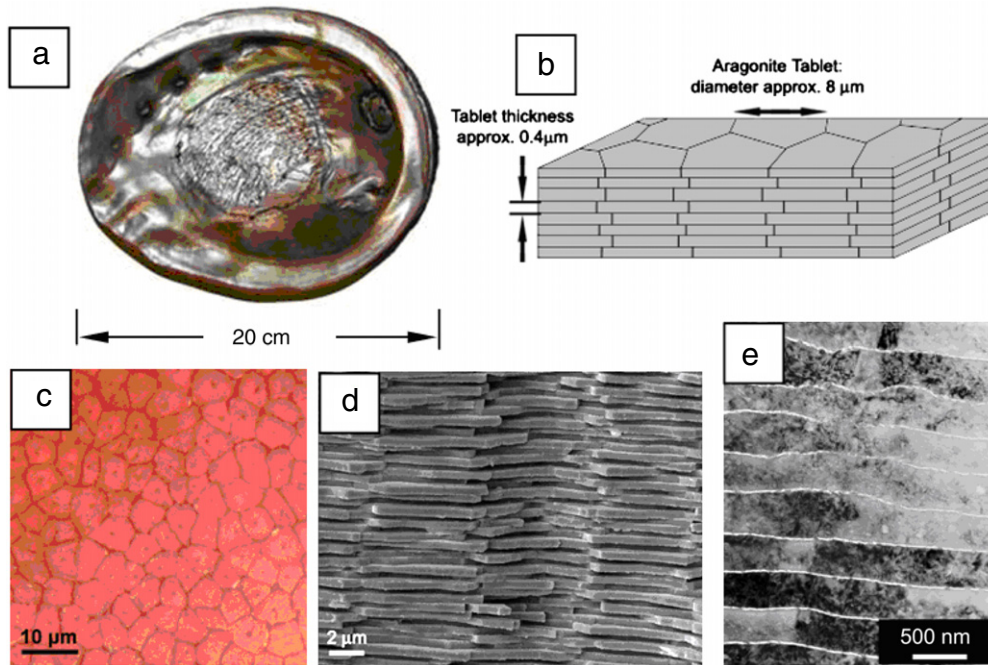


Fig. 1 – The multiscale structure of nacre from red abalone: (a) inside view of the shell, (b) schematic of the brick wall like microstructure, (c) optical micrograph showing the tiling of the tablets, (d) SEM of a fracture surface, (e) TEM showing tablet waviness.

Source: Reproduced from Ref. [Barthelat et al. \(2007\)](#).

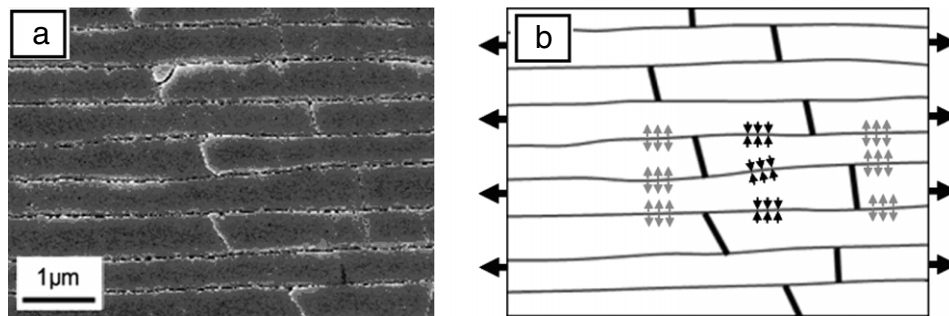


Fig. 2 – (a) Scanning electron micrographs of a few dovetail-like features at the periphery of the tablets. (b) Outline of the tablets contours, showing some of the stresses involved when nacre is stretched along the tablets. In addition to shear the interface is subjected to normal compression (black arrows) which generates resistance to tablet pullout. Equilibrium of forces at the interfaces requires tensile tractions at the core of the tablets.

Source: Reproduced with permission from [Barthelat and Espinosa \(2007\)](#).

the layers. The transition from elastic to inelastic behavior is progressive (rounding of the curve), which probably results from the statistics of the microstructure. Unloading paths show a decrease in modulus, which indicates a progressive accumulation of damage. The tensile behavior of aragonite is also shown on that graph: linear elastic deformation followed by sudden, brittle failure at small strains. Nacre, although made of 95% of that mineral, exhibits a ductile-like behavior with relatively large strain at failure.

This remarkable behavior is achieved by the following microscopic mechanism: At a tensile stress of about 60 MPa the interfaces start to yield in shear and the tablets slide on one another, generating local deformation. This phenomenon

spreads over large volumes throughout the specimen, which translates into relatively large strains at the macroscale. Once the potential sliding sites are exhausted, the specimen fails by pullout of the tablets (see fracture surface, [Fig. 1\(d\)](#)), which occurs after local sliding distances of 100–200 nm. This type of micromechanism is unique to nacre, and it is the main source of its superior mechanical properties.

In order to achieve such behavior, however, some requirements must be met. First, the interface must be weaker than the tablets; otherwise, the tablets would fail in tension before any sliding could occur, which would lead to a brittle type of failure. Strong tablets are important in this regard, and it was shown that their small size confers them

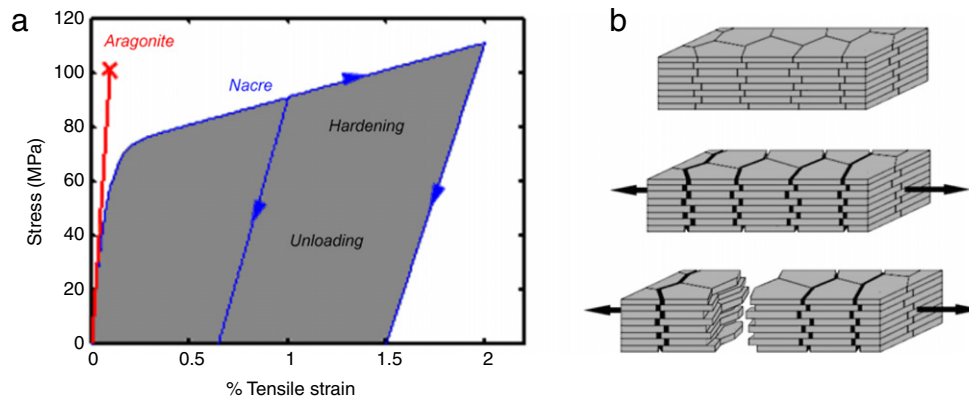


Fig. 3 – Experimental tensile stress–strain curve for nacre and (b) associated deformation modes.

Source: Reproduced from Ref. [Barthelat and Espinosa \(2007\)](#).

with increased tensile strength compared to bulk aragonite ([Currey, 1977](#); [Gao et al., 2003](#)). It has also been suggested that the presence of nanograins provides some ductility to the tablets ([Li et al., 2006](#)). This would increase the tensile strength of the tablets, but would not significantly affect the deformation mode of nacre, which is dominated by tablet sliding. In addition, the aspect ratio of the tablets must be high enough to maximize sliding areas and produce strong cohesion within the material ([Ji and Gao, 2004](#)). However, the aspect ratio is bounded by the fact that too thin tablets would lead to premature tablet failure and brittle behavior. Another fundamental requirement is that some hardening mechanism must take place at the local scale in order to spread sliding throughout the material. As tablets start to slide, higher stresses are required to slide them further so that it is more favorable for the material to initiate new sliding sites, thus spreading deformation over large volumes. Since the tablets remain essentially elastic in this process, the hardening mechanism has to take place at the interfaces. Strain hardening is the key to large deformation and is essential to the mechanical performance of nacre.

A large class of biomimetic materials and organic/inorganic composites that aim to reproduce the mechanical properties of nacre have been developed and studied ([Ortiz and Boyce, 2008](#)). Mimicking the intricate microstructure and deformation mechanisms of nacre is a challenge that requires both the design of an optimum microstructure and the development of fabrication procedures to implement this design. A variety of fabrication methods including self-assembly ([Heuer et al., 1992](#); [Sellinger et al., 1998](#); [Zhang et al., 2006](#)), layer-by-layer assembly or sequential deposition ([Bonderer et al., 2008](#); [He et al., 1997](#); [Kato, 2000](#); [Podsiadlo et al., 2007a,b](#); [Tang et al., 2003](#); [Wei et al., 2007](#)), ice-templating ([Deville et al., 2006](#)), and microfabrication ([Chen et al., 2007b](#)), have been proposed and tested for nacre-inspired materials, with the goal of demonstrating increases in strength and toughness of composites that utilize the deformation mechanisms of nacre. However, limitations in precise spatial control in 3 dimensions as encountered by these methods, mean that many of the fabricated

composites do not display the microstructural characteristics of nacre beyond the layered organic/inorganic structure ([He et al., 1997](#); [Kato, 2000](#); [Sellinger et al., 1998](#); [Wei et al., 2007](#); [Zhang et al., 2006](#)). Furthermore, damage spreading,

essential to the toughness achieved in abalone shells, has not yet been demonstrated in these artificial composites. For the layered composites of hard tablets embedded in a soft matrix ([Bonderer et al., 2008](#); [Podsiadlo et al., 2007a,b](#)), the volume fraction of the tablets achieved are too low for the hardening mechanisms observed in nacre to take place ([Barthelat and Espinosa, 2007](#); [Barthelat et al., 2009](#)), and thus they depend on the tablet-matrix adhesion and the stiffening/toughness of the polymers for an increase in toughness. To realize the full potential of nacre-inspired composites, specifically the orders of magnitude increase in toughness, the contributions from the small length scale features observed in nacre, namely the close-packed tablets and the nanostructure of the tablets, such as mineral bridges and tablet waviness, need to be captured. In fact, biomimetic material design and optimization require the fine-tuning of small scale parameters and material properties (optimization space) that are ultimately represented by the desired macroscopic performance (objective function). These performance metrics usually operate at length scales that are orders of magnitude larger than, and at higher hierarchical levels, than the scales at which those parameters and properties interact. The challenges associated with such problems are associated to understanding the mechanics of the material's deformation and failure at the most relevant length scales and the study of their effect of material properties at the higher length scales, which can only be addressed with appropriate multiscale strategies. For instance, nacre presents only two levels of hierarchy ([Currey, 1977](#)), and the effect of hierarchy has been discussed in [Gao et al. \(2003\)](#), [Ji and Gao \(2004\)](#) and [Pugno \(2006\)](#).

The objective of our work is to identify the right mechanisms at the lower scale that control the material behavior at the higher scale, and in such way determine the material properties and performance from microstructural descriptors. In this way, we claim that our approach is multiscale in the sense that we intend to bridge the most relevant length scales in the mechanics of nacre-like materials.

In addition, lack of manufacturing precision in spatial dimensions and surface features make it impossible to carry out a systematic study and analysis of the design parameters directly, which is necessary to fully understand the interplay between microstructural and material parameters that leads

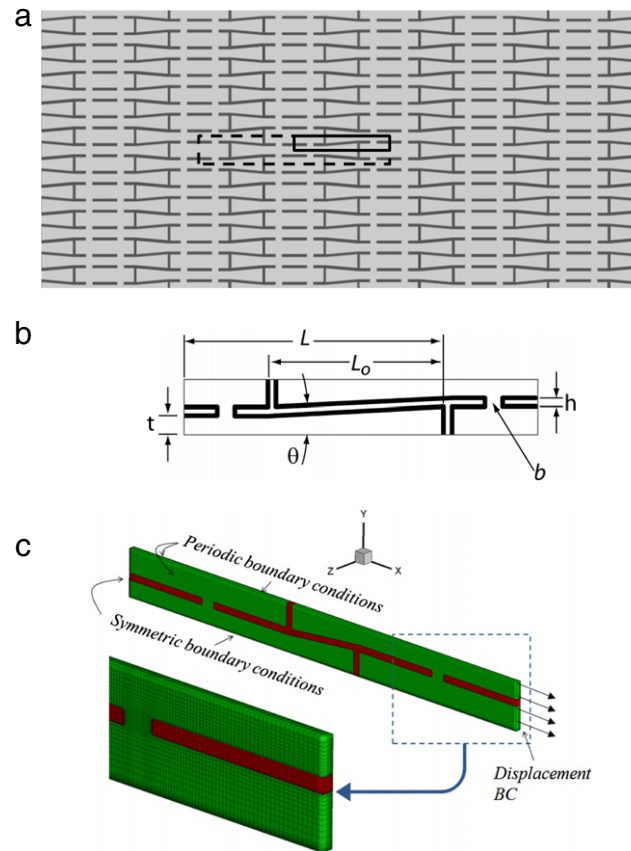


Fig. 4 – (a) A periodic structure for artificial nacre, and (b) a unit cell of the structure with geometric parameters. (c) Details of the finite element model.

to the performance of nacre. In order to address this limitation, a design for artificial nacre that incorporates the abovementioned features is proposed, and systematic numerical analysis of the design parameter space is carried out. It is shown through numerical analysis that in order to replicate the deformation mechanisms of nacre, a delicate balance must be struck between the geometry and arrangement of the structure and the properties of the constituent materials. A parametric analysis of the structural and material design specifications is undertaken in order to identify the optimal configuration.

Finally to implement this design, rapid prototyped samples through fused deposition modeling, are created with the same design specifications defined in the numerical analysis. This allows for precise three-dimensional control of the geometry. A parametric study is also conducted where we determine optimal design parameters. Furthermore we discuss the similarities between numerical analysis and experiments while relating these results to the failure mechanisms of natural nacre.

2. Parametric analysis of artificial nacre

2.1. Geometry

Our design of artificial nacre is based on [Espinosa and Barthelat \(2007\)](#), [Espinosa et al. \(2009\)](#) and [Fig. 4\(a\)](#). The design

exhibits the features that lead to the unique deformation mechanisms present in nacre. Brittle tablets and ductile polymer filler is used in our two-constituent composite model. The waviness of the tablets in nacre that leads to locking and damage distribution is incorporated into the model through a dovetail tablet design, [Espinosa and Barthelat \(2007\)](#), with an angle θ . Columnar bridges are introduced to connect the individual tablets vertically and maintain cohesion of the microstructure ([Barthelat et al., 2007](#)). A representative periodic cell is shown with dashed lines in [Fig. 4\(a\)](#). To simplify our calculations, only a quarter of a single periodic unit cell is considered (shown as solid lines). The unit cell has a cross-section as shown in [Fig. 4\(b\)](#), and is uniform throughout the thickness.

The 2-D periodic structure is defined by six geometric parameters: the length of a tablet L , the length of overlap between tablets L_o , the dovetail angle θ , the tablet thickness, t , the thickness of the bridge, b , and the thickness of the filler, h . These geometrical values are listed in [Table 1](#).

2.2. Computational model

In order to exploit periodicity, we investigate uniaxial tension along the directions of the tablets, which is one of the most relevant modes of deformation. *Abaqus Standard FEM* code v6.7 is used to simulate the unit cell under uniaxial loading. All the boundaries that are not actively loaded are under

Table 1 – Unit cell geometric parameters.

L	2 mm
L_0	0.2–1.2 mm
θ	0° – 9°
t	0.12 mm
b	0.1 mm
h	0.05 mm

Table 2 – Material parameters from Granta CES Edupack Material Selection Software (2010).

Tablet	E^T	σ_f^T	ν^T
ABS	1.5 GPa	65 MPa	0.41
Aluminum alloy	60 GPa	310 MPa	0.33
Alumina	300 GPa	350 MPa	0.21
Filler	E^F	σ_y^F	ν^F
Chitosan	2 GPa	40 MPa	0.4

periodic boundary conditions. The tablets are elastic, the filler is elastic–perfectly plastic, and the interface between the tablets and filler is modeled with cohesive elements with progressive damage. The representative geometry of the unit cell is shown in Fig. 4(b). A 3D finite element mesh based on this unit cell is shown in Fig. 4(c). The mesh represents a slide of the extruded 2D periodic array in Fig. 4(a), where the green region represents the tablet and the red region the filler material. Periodic boundary conditions are applied at the front, back and top faces as indicated by arrows in Fig. 4(c). We also note that this unit cell is actually one quarter of the simplest periodic unit cell, and therefore, it is necessary to apply symmetric boundary on the bottom and left faces. Displacement boundary conditions are applied only at the nodes located at the right face as shown by arrows in the figure.

2.3. Material and interface models

The artificial composite investigated is comprised of two very different materials: the brittle tablets, and the ductile organic filler between the tablets. Hence, the material models were chosen to be linear elastic for the tablets and elastic–perfectly plastic for the filler.

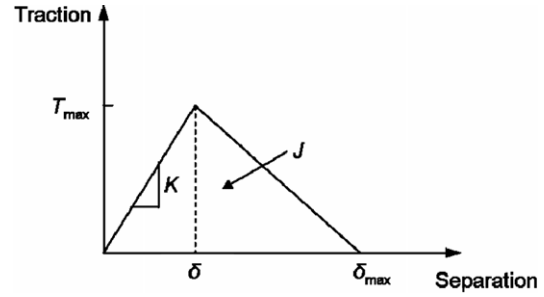
$$\text{Tablet: } \sigma^T = E^T \varepsilon^T; \quad \sigma^T \leq \sigma_f^T \quad (1a)$$

$$\text{Filler: } \begin{cases} \sigma^F = E^F \varepsilon^F & \text{for } \varepsilon^F < \varepsilon_e^F \\ \sigma^F = \sigma_y^F & \text{for } \varepsilon^F \geq \varepsilon_e^F, \end{cases} \quad (1b)$$

where the filler's yield stress is given by $\sigma_y^F = E^F \varepsilon_e^F$. The strength of the tablet is σ_f^T , and the Poisson's ratios of the tablet and filler materials are ν^T and ν^F , respectively (Table 2).

Three tablet materials, alumina, an aluminum alloy and ABS, and chitosan as the filler material are considered. The tablet materials were chosen to represent a wide range of stiffness and strength. The filler material was chosen for its biological origin (chitosan), as well as its small stiffness and yield strength. The material parameters and geometric dimensions of the unit cell are given in Tables 1 and 2.

The adhesion of the tablets and filler is modeled with a traction–displacement cohesive relation at the interface, as

**Fig. 5 – Cohesive traction–separation law for the interface.****Table 3 – Values of interface parameters.**

K	1000 MPa/mm
T_{\max}	0.5–5 MPa (0.5)
J	0.01–1 mJ (0.01)
μ	0.1

shown Fig. 5. An initial linear response is followed by a linear evolution of material damage once the maximum stress is reached. The model is defined by three parameters for each of the normal and tangential loading directions: the initial stiffness K , the maximum traction T_{\max} , and the fracture energy J (area under the traction–separation curve). K and J have units of stress per unit length and energy per unit area, respectively (Table 3). For simplicity, an isotropic cohesive law is considered where the constitutive behavior is identical in the normal and tangential directions. After decohesion, the filler–tablet interface is modeled by the Coulomb friction law with a friction coefficient of μ .

2.4. Mechanical response of the unit cell under tension

Snapshots of the dovetail region under increasing levels of uniaxial tensile loading are shown in Fig. 6. As the tablets are pulled apart, the initial resistance comes mainly from the adhesion between the tablets and filler. According to the cohesive law shown in Fig. 5, the stress in the cohesive elements increases until T_{\max} is reached, after which the interface traction drops continuously to zero (Fig. 6(a) and (b)).

This sequence of events results in the characteristic tensile stress–strain curves plotted in Fig. 7. The stress plotted in Fig. 7, is directly computed as the average of the normal stresses at the end surface of the unit cell. The strain is the macroscopic displacement of the unit cell end surfaces divided by the initial length. It is worth noting that stress increases during loading can offset by the decrease in the overlap area as the tablets move further apart (Fig. 6(c) and (d)).

Fig. 7(a) shows two stress–strain curves of the ABS–chitosan system. The initial rise and drop in stress of curve ABS1 is associated with the interface adhesion. Relative to the filler yield stress, the interface parameters for ABS1 are $T_{\max}/\sigma_y^F = 0.0125$ and $J/(\sigma_y^F L) = 0.0005$. Once the cohesive elements have failed, i.e., the adhesion of the tablet and filler is overcome, the stress rises again due to the locking effect of the dovetail in the tablets. Curve ABS2 shows the response of

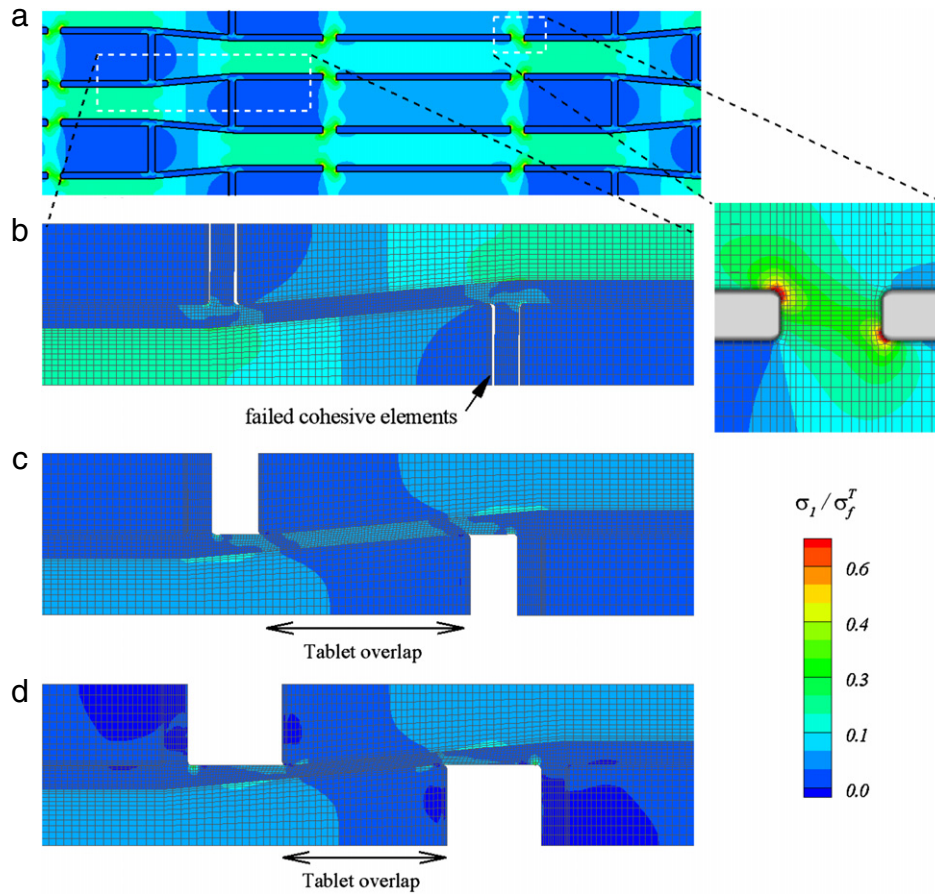


Fig. 6 – Evolution of the unit cell dovetail region and contour plots of Max. principal stress to tablet strength ratio σ_1/σ_f^T as the loading proceeds. (a) The cohesive elements deform under tension; (b) parts of the cohesive elements fail completely; (c) and (d) tablet overlap area, under compression, decreases as the tablets move further apart. (For interpretation of the references to colour in this figure legend, the reader is referred to the web version of this article.)

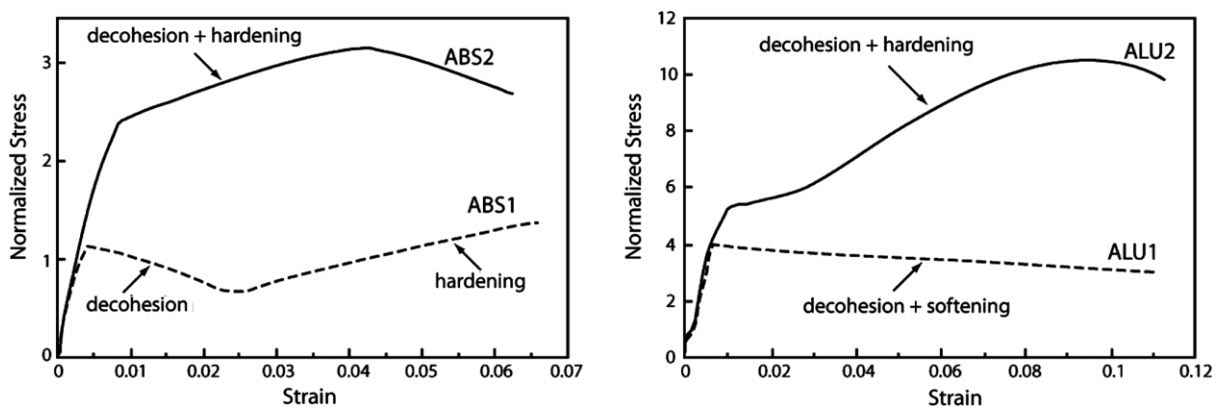


Fig. 7 – Two typical uniaxial stress-strain curves of the ABS-chitosan system (right) and alumina-chitosan system (left).

a system with a stronger tablet-filler interface. For ABS2 the interface parameters are $T_{\max}/\sigma_y^F = 0.025$ and $J/(\sigma_y^F L) = 0.05$. Here, the initial rapid rise in stress is followed by a more gradual increase in stress as the interface elements degrade progressively. The stronger cohesion means that stresses increase to comparable levels to those at the interface, before

the interface degradation causes the stress to decrease, as it happens in ABS1. The drop in stress at larger strain in ABS2 is caused by the decrease in the area of overlap, or the region of lateral compressive stress, as the tablets are pulled apart.

The responses of the alumina-chitosan system, shown in Fig. 7(b), exhibit different characteristics. In this case,

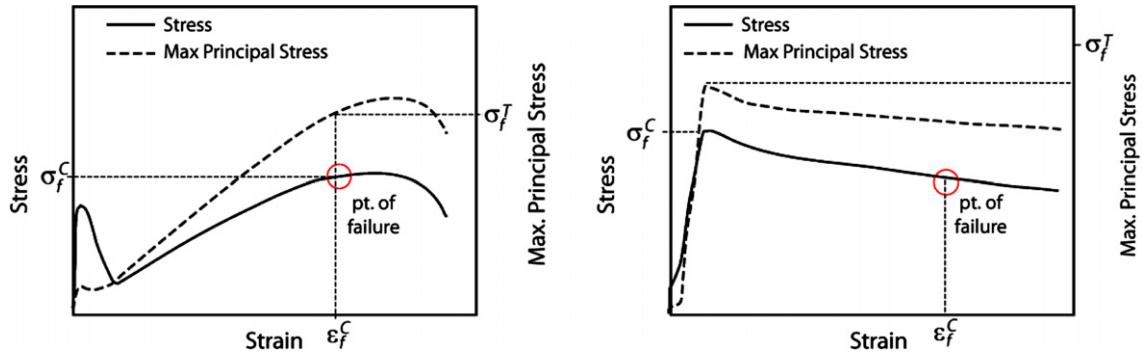


Fig. 8 – Examples of failure modes and points of failure: stress hardening and failure by tablet fracture (left), and stress softening and failure by tablet pullout (right). The solid curves indicate average system stress, and the dashed curves indicate the maximum principal stress in the tablets. The area under the stress curves for $e \leq e_f^C$ is equal to U^C .

interface parameter values are the same for the ALU1 and ALU2 material. However, the overlap lengths are different: $L_0/L = 0.5$ for ALU1, and $L_0/L = 0.6$ for ALU2. Curve ALU1 shows a sharp increase in stress followed by a softening brought about by the yielding of the filler; while curve ALU2 shows a continuous increase in stress, indicating hardening, up to a peak value followed by softening. The transition from the first curve to the second occurs when the tablets experience larger stress, larger dovetail overlap length, where the tablets and polymer sustain compressive stresses over a larger area. This compensates for the yielding in the filler which acts to lower the average stress. The transverse strains for both systems (not shown) display an initial contraction due to the Poisson effect of the tablet and filler, and subsequent expansion due to the tablets climbing over the incline angle, as seen in experiments on biological nacre (Barthelat and Espinosa, 2007; Barthelat et al., 2006, 2009, 2007).

These results reveal a characteristic of the macroscopic stress–strain behavior in which stress hardening or softening may occur as a function of the constituent properties and those of the interface between them. In our classification of the phenomenon, stress hardening describes the increase in stress after an initial almost linear regime that is sometimes followed by a decrease in the average stresses, examples of which are shown in Fig. 7(a) and (b). Note in particular, the similarities between Fig. 3(a) and ABS2 of Fig. 7(a). We refer as stress softening to those systems where an initial maximum stress occurs at strains smaller than 0.03, followed by a monotonic decrease in stress; a typical softening stress–strain curve is ALU1 of Fig. 7(b). There is an intermediate case of softening and hardening as seen in the stress–strain curve ABS1 in Fig. 7(a). Note that the monotonic decrease after a maximum stress in ABS2 of Fig. 7(a) is still classified as stress hardening as the maximum stress occurs at a strain considerably larger than 0.03.

The different failure modes of the artificial material can be classified largely into tablet pullout and tablet fracture. Failure through tablet fracture is defined via a brittle fracture criterion: the tablet fails at the point where the maximum principal stress exceeds its strength: $\max_{\text{tablet}} \sigma_1^T > \sigma_f^T$. In our simulations, when tablets fracture, it always occurred at the bridge. Tablet pullout occurs when the strength of the tablet

is not exceeded throughout the simulation: $\max_{\text{tablet}} \sigma_1^T < \sigma_f^T$. In this case, the point of failure is defined to be at a strain of 0.1. The value 0.1 is chosen to be much larger than the strains real nacre can sustain, and sufficiently small to make the simulations more effective without affecting our results and conclusions. The strain energy then is underestimated for tablet pullout, as a complete pullout of the tablet occurs at a strain larger than 0.1.

Examples of the two different failure modes and points of failure are shown in Fig. 8. The macroscopic tensile behavior of the unit cell can be described by a combination of stress hardening/stress softening and failure by tablet fracture/tablet pullout. Fig. 8(a) shows a stress hardening/tablet fracture mode, while Fig. 8(b) shows a stress softening/tablet pullout mode.

The performance of the composite can be gauged by two parameters: the maximum stress up to failure, σ_f^C , and the strain energy absorbed by the composite U^C . The definition of σ_f^C is quite straightforward: it is the maximum stress that the composite can sustain before failing. The strain energy U^C is defined to be the area under the composite stress–strain curve up to the strain at which the composite fails, determined as above. In general, the combination of stress hardening and tablet pullout results in the largest values of σ_f^C and U^C .

2.5. Parametric analysis

It was demonstrated in the previous section that depending on the selected materials for tablet and filler and/or unit cell interface properties and geometric dimensions, quite different composite behaviors may be obtained. In order to address the design problem in a systematic way, we conduct a parametric analysis with respect to the interface and geometric parameters. Our performance metrics are the macroscopic maximum stress to failure σ_f^C , and the energy dissipation density U^C , up to failure. In other words, the objective of the analysis is to optimize the material and geometric parameters of the system, in order to maximize σ_f^C and U^C . In particular, a large dissipated energy is desirable as it correlates to the fracture toughness (Barthelat and Espinosa, 2007).

Table 4 – Dimensionless material parameters for tablet-filler pairs considered.

Tablet	Filler	E^F/E^T	σ_f^T/E^T	σ_y^F/E^T	σ_y^F/σ_f^T
ABS	Chitosan	1.33	0.0433	0.0267	0.61
Aluminum alloy	Chitosan	0.0333	0.0517	6.67×10^{-4}	0.12
Alumina	Chitosan	6.67×10^{-3}	1.17×10^{-3}	1.33×10^{-4}	0.11

The material and interface parameters of the problem are $E^T, E^F, \sigma_f^T, \sigma_y^F, \nu^T, \nu^F, \mu, K, T_{\max}$, and J . In addition, the geometric parameters are L, L_o, θ, t, b , and h (Table 1). Dimensionless parameters are obtained by expressing them as a combination of two fundamental physical quantities: force and distance. The variables can thus be written in dimensionless form as $E^F/E^T, \sigma_f^T/E^T, \sigma_y^F/E^T, KL/E^T, T_{\max}/\sigma_f^T, E^FJ/T_{\max}^2L, \nu^T, \nu^F$, and μ for the material parameters, and $\theta, L_o/L, t/L, b/L$, and h/L for the geometric parameters. The parameter space in total consists of 14 independent dimensionless variables.

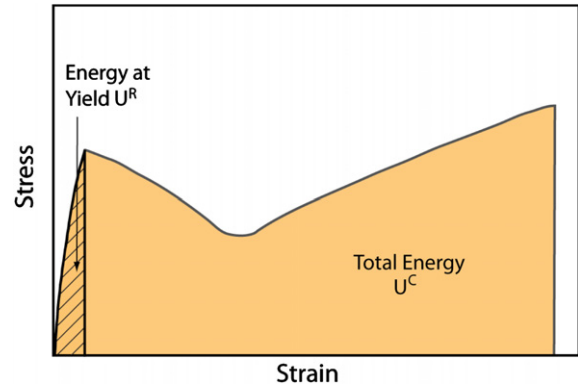
The analysis of the effect of the various geometrical and material parameters involved in the mechanics of nacre could be very exhaustive. Although it would be desirable to write an explicit functional form for the macroscopic mechanical response of the artificial nacre structure as a function of all the microstructural variables, such a task is extremely difficult if not impossible. However, we interrogate this function numerically by looking at suitable projections involving relationships between selected parameters in order to better understand how these relationships could conceivably be used for the design of artificial nacre microstructures in response to the applied load. To that end, the dimensional analysis proposed here could be a powerful tool to undertake such a complex task. First, we restrict the material choices, $E^F/E^T, \sigma_f^T/E^T$ and σ_y^F/E^T to the three values given in Table 4. Further, the variable space can be considerably reduced by carefully considering the relevance of each variable to the output results. For instance, the Poisson's ratios for the tablet and filler materials typically range between 0.2 and 0.4, and are not expected to have a significant effect on the output variables of interest. In addition, the friction coefficient between the tablet and filler material is not expected to vary much, and so this value is kept constant at 0.1. Among the geometric parameters, we focus on $\theta, L_o/L$, and b/L as preliminary calculations showed these to have the largest impact on σ_f^C and U^C .

For the energy normalization, the total energy of the composite material, U^C , will be compared to a reference value of energy at yield of the composite with a zero degree dovetail angle, U^R . This serves as a good metric for normalization since the zero degree dovetail angle composite yields when the filler material yields. A schematic of this representation is seen in Fig. 9. From Fig. 9 we can calculate the normalized energy U^C/U^R . Reference values for U^R and σ^R are seen in Table 5.

The relationships to be identified are therefore

$$\frac{\sigma_f^C}{\sigma_f^R} = f \left(\frac{E^F}{E^T}, \frac{\sigma_f^T}{E^T}, \frac{\sigma_y^F}{E^T}, \frac{T_{\max}}{\sigma_f^T}, \frac{E^FJ}{T_{\max}^2L}, \theta, \frac{L_o}{L}, \frac{b}{L} \right)$$

$$\frac{U^C}{U^R} = g \left(\frac{E^F}{E^T}, \frac{\sigma_f^T}{E^T}, \frac{\sigma_y^F}{E^T}, \frac{T_{\max}}{\sigma_f^T}, \frac{E^FJ}{T_{\max}^2L}, \theta, \frac{L_o}{L}, \frac{b}{L} \right).$$

**Fig. 9 – Schematic of total energy dissipation and energy at yield, which is used in the normalization.****Table 5 – Failure stress and dissipated energy for the reference monolithic cell of tablet material.**

Tablet	σ_f^R (MPa)	U^R (mJ/m ³)
ABS	3.4	0.012
Aluminum alloy	3.16	0.0364
Alumina	3.2	0.00943

The stress–strain response that is required in an artificial nacre material is that of increasing stress with strain, or hardening behavior. This implies that tablets do progressively “lock”, thus distributing the damage over a large number of tablets. At the same time, the stresses in the tablets should not exceed the strength of the material, therefore resisting tablet fracture. Too much hardening leads to higher stresses in the tablet and failure at an earlier strain. Hence, there is an optimum in the space of independent variables.

2.5.1. Effect of dovetail angle θ and overlap length L .

The dovetail angle, θ , has a large effect on the output variables, composite strength and dissipated energy, as seen in Fig. 10. In general, σ_f^C/σ_f^R tends to increase with θ while U^C/U^R reaches a peak at small θ then decreases as θ becomes larger. Henceforth, any parameters that are not explicitly mentioned will assume the reference values given in Table 1.

Fig. 10 shows that $\sigma_f^C/\sigma_f^R > 1$ for both ABS-chitosan and alumina-chitosan systems. In these plots, the various mechanisms: softening–pull out (s/p), hardening–pull out (h/p), and hardening–failure (h/f) are labeled in selected cases. For the ABS composite material, σ_f^C/σ_f^R varies from 1 to 1.6 implying that the maximum stress in the composite is only 60% greater than the composite yield stress. Conversely, σ_f^C/σ_f^R for the alumina composite material varies from 1 to 4.3 meaning the strength of the composite is over 300% greater than the yield strength. For this reason, the energy

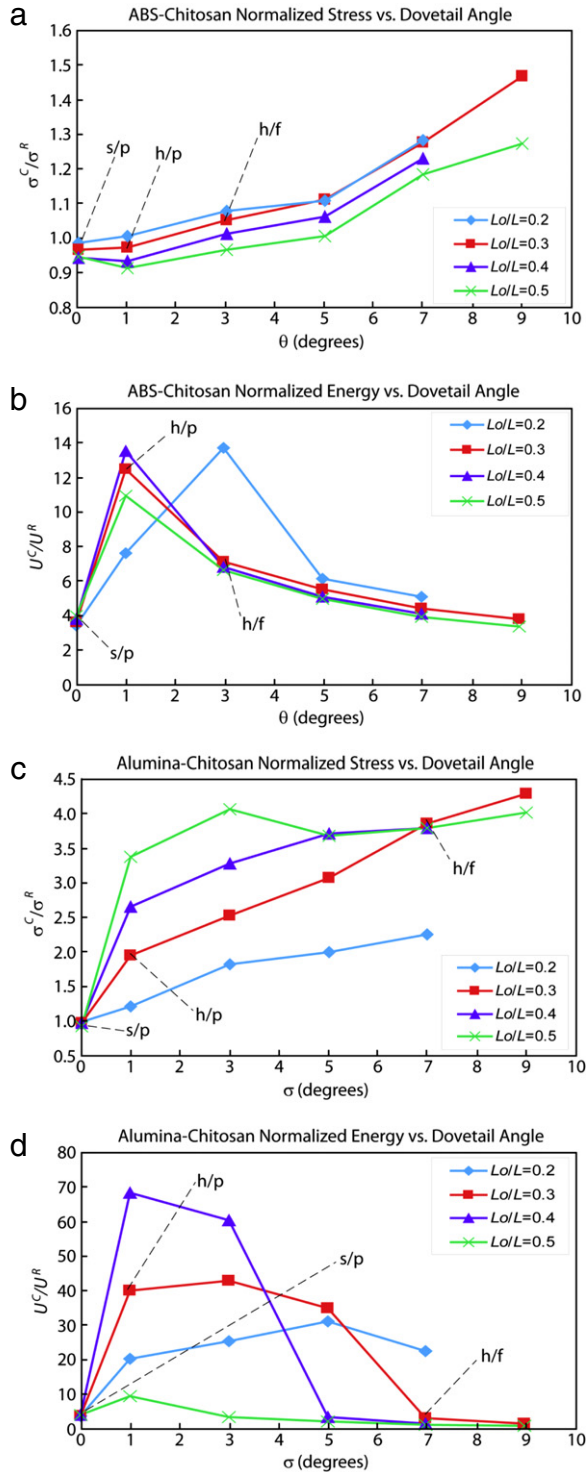


Fig. 10 – (a) σ_f^C/σ_f^R and (b) U^C/U^R of the ABS-chitosan system and (c) σ_f^C/σ_f^R and (d) U^C/U^R of the alumina-chitosan system as θ is increased, for L_o/L values of 0.2, 0.3, 0.4, and 0.5. A specific case of $L_o/L = 0.3$ (red curve) was chosen to show failure mode transitions of softening pullout (s/p), hardening pullout (h/p), and hardening fracture (h/f). Failure mode transitions for other values of L_o/L can be seen in Fig. 11. (For interpretation of the references to colour in this figure legend, the reader is referred to the web version of this article.).

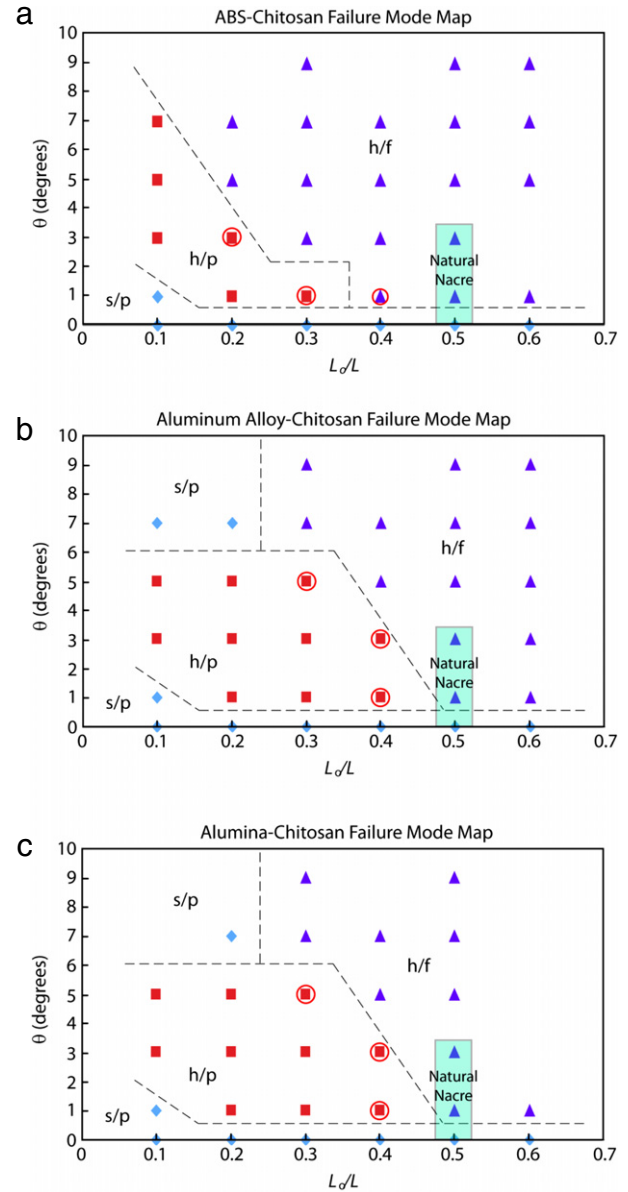


Fig. 11 – Map of softening/pullout, hardening/pullout, and hardening/fracture stress responses in the $\theta - L_o/L$ space for the (a) ABS-chitosan, (b) aluminum alloy-chitosan, and (c) alumina-chitosan systems. The symbols are the actual data points. The three points with the largest energy dissipation in each map are circled in red. All maps show the failure mode of natural nacre. (For interpretation of the references to colour in this figure legend, the reader is referred to the web version of this article.)

dissipation, U^C/U^R , is five times greater for the alumina composite than the ABS composite.

The failure mode of each $(\theta, L_o/L)$ combination shown in Fig. 10 is plotted in Fig. 11. For $\theta = 0$, stress will always soften, since the lack of tablet confinement means that once the tablet-filler interface has failed, there is no mechanism for stress buildup in the system. Likewise, for small L_o/L and small θ , the stresses in the system are small enough for stress softening to occur. The main transition in the ABS-chitosan

system for $L_0/L < 0.5$ is between hardening/fracture and hardening/pullout. The absence of stress softening behavior other than for $\theta \approx 0$ is due to the weak tablet material and weak adhesion between the tablet and filler—the stresses on the filler never reach the yielding point. Tablet pullout tends to occur at smaller L_0/L and θ values as expected, where the stresses in the system are smaller. The smaller L_0/L is, the larger θ can be while still maintaining small enough stresses for tablet pullout. Note that the largest values of U^C/U^R occur at those points where tablet pullout is on the brink of transitioning to tablet fracture. At these points, the tablets are capable of withstanding the maximum local stress without fracturing.

By contrast, in the alumina-chitosan system (and also in the aluminum alloy-chitosan system), more than one transition occurs depending on the values of θ and L_0/L (other than the softening for $\theta \approx 0$); At small enough system stresses, with small to intermediate θ and L_0/L values, hardening occurs since the filler does not yield until a later stage in the simulation, as in the ABS-chitosan system. The strong alumina is able to sustain relatively higher levels of stress at these θ and L_0/L values, and the system fails by tablet pullout. Softening/pullout occurs at intermediate stress levels, at larger θ and smaller L_0/L values, where larger stresses in the hard alumina causes the filler to yield early on in the simulation but the increase in stresses in the tablets is not quite enough to overcome the decrease in overlap area as the tablets are pulled apart. This changes as the stresses in the system increase with increasing θ and/or L_0/L values; progressive locking of the overlap regions is sufficient to cause hardening and tablet fracture. The values of U^C/U^R are consistently larger at those points where tablet pullout occurs; they are drastically smaller where the composite fails by tablet fracture. The increase in dissipated energy for the alumina-chitosan composite is then mainly due to the “ductility” conferred by the filler. In other words, the ability to sustain large strains without fracturing the tablets is key to the increased toughness of artificial nacre materials.

2.5.2. Transitions between characteristic behaviors

As noted in the previous sections, the particular combination of stress hardening/softening and failure by tablet pullout/tablet fracture is an important characteristic of the macroscopic stress-strain behavior, and has a large impact on the resulting values of σ_f^C/σ_f^R and U^C/U^R . In addition, the interplay of the various parameters means that the behavior of the system cannot simply be deduced by considering the individual parameters separately. In order to demonstrate this, a diagram of the different failure modes in the variable space, can be constructed. Softening/tablet pullout (s/p), hardening/tablet pullout (h/p), and hardening/tablet fracture (h/f) regions are shown in Fig. 11 in the $\theta - L_0/L$ space for the ABS-chitosan, aluminum alloy-chitosan, and alumina-chitosan systems. These maps are drawn from the data points that are also shown in Fig. 10. Note that the boundaries of the maps are approximate, especially in the regions where there are insufficient data points to unambiguously determine the boundaries. However, the clustering of the data points for the different macroscopic responses indicate that in general, stress softening and tablet pullout occur at smaller values of

θ and L_0/L , while hardening and tablet fracture occur at larger values of θ and L_0/L .

E^F/E^T and σ_y^F/E^T decrease as the tablets become stiffer from ABS to the aluminum alloy and alumina. The maps of aluminum alloy-chitosan and alumina-chitosan are very similar; the exact boundaries might differ as the depicted boundaries are estimations. The map of ABS-chitosan is quite different from the other two. As the tablet changes from ABS to alumina, tablet pullout extends to higher values of θ at constant L_0/L . On the other hand, stress softening occurs in the upper left corner, where θ is large while L_0/L is small. Note that the softening in this region is due to the yielding of the filler at small strains, while the softening in the lower part of the map is due to the small stresses in the composite when θ and L_0/L are very small. The larger h/p region in the aluminum alloy-chitosan and alumina-chitosan maps indicates the benefit of using stiffer tablet materials.

We note that the circled points in Fig. 11 represent those geometries that exhibit the largest energy dissipation without sacrificing strength (from Fig. 10). In our view, these geometries represent well the targeted composites. As shown in Fig. 11, these points fall at the boundary between hardening/tablet pullout and hardening/tablet fracture, which supports the fact that the most favorable mechanical performance is actually achieved as the optimization between two competing mechanisms. For instance, in the case of alumina-chitosan, the points marked with circles correspond to those cases that exhibit the largest energy dissipation (Fig. 10(d)) and high strength (Fig. 10(c)): two for $L_0/L = 0.4$ and one for $L_0/L = 0$. In particular, the case with $L_0/L = 0.4$ and $\theta = 1^\circ$ gives the best energy dissipation without sacrificing strength, and will be used in future discussions.

As we also included the dovetail angle and overlap distribution found in natural nacre (shown as light blue rectangles in Fig. 11(a)–(c)), we observed that they fall remarkably close to our highest performing geometries. We surmise that the low young modulus of the ABS compared with the chitosan makes the optimum geometry of the ABS-chitosan system to be slightly different from the natural nacre, since we are actually moving away from the ideal stiff tablet-soft interface nacre-inspired model. However, our results with the alumina-chitosan and aluminum alloy-chitosan system suggest that our bioinspired parametric study arrived at a similarly optimized design to that of Nature's evolution process.

3. Size effects

The parametric analysis on the artificial nacre described in the previous section (Section 2.5) was presented using a fixed normalization energy and strength. Although, this analysis is very helpful to find the optimum geometry for any given material system, little information can be obtained about the real benefit of making these composite microstructures. In this section, this benefit will be measured in terms of the mechanical response of the composite material compared with those of the monolithic material at specific length scales.

As previously discussed, naturally occurring nacre (95% aragonite) is usually contrasted with its monolithic counterpart, geological aragonite (Barthelat et al., 2007). Fig. 12 shows

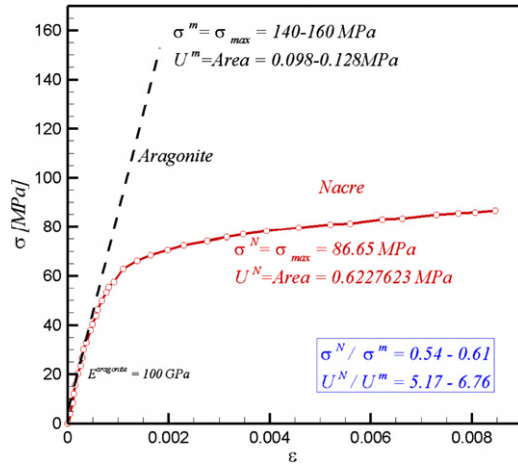


Fig. 12 – Stress–strain curve of nacre in tension along the tablets.

the experimental uniaxial stress–strain curve of geological aragonite and naturally occurring nacre, in which it can be inferred that, albeit the ratio of tensile strength of the nacre to that of the monolithic aragonite is $\sigma^N/\sigma^m = 0.54\text{--}0.61$, the consequent energy gain could reach $U^N/U^m = 5.17\text{--}6.76$. Espinosa and co-workers (Barthelat and Espinosa, 2007; Barthelat et al., 2007) have shown that this increase in energy and inelastic behavior with hardening in nacre is a key contributor to the 1000-fold increase in fracture toughness. In fact, nacre achieves this increase in energy, without significantly sacrificing its stiffness, by means of its microstructural design. It may seem tempting to draw an analogy comparing the results discussed in Section 2.5 with the strength of the tablet material as well. However, the composite strength and energy improvement over that of the monolithic material using the strength reported in Table 2 would not lead to similar results as nacre. (e.g., the strength of the composite to the strength of alumina would only be $\sigma^C/\sigma_f^T = 0.0242$, and the energy improvement $U^C/U_f^T = 0.0242$, where $U_f^T = (\sigma_f^T)^2/(2E^T)$). However, such a comparison would not be meaningful, since σ_f^T , used in the previous section, represents the strength of the mineral bridge and not that of the monolithic material for a macroscopic sample. On the other hand, the strength of aragonite, shown in Fig. 12, is not representative of the strength in the mineral bridges of the naturally occurring nacre. To make appropriate comparisons in strength and energy, size effects need to be included in the analysis. In this analysis, a simple scaling law based on Weibull statistics is used.

Size effects on the mechanical response of biomineralized materials was first discussed by Gao et al. (2003) who claimed that the theoretical strength of aragonite can only be achieved at a critical length scale (around $h^* = 30$ nm). Although they speculated that the tablets were insensitive to cracks, that argument was later refuted by Ballarini et al. (2005) and Ruoff and Pugno (2005) who argued that the mineral phase of the tablets can be indeed sensitive to flaws. In our analysis we consider the mineral phase to obey Weibull statistics (Bazant and Chen, 1997; Peng et al., 2006; Weibull, 1951). This simple scaling law can later be extended to consider the transition from Weibull to strength based criterion (in

the case where the tablets/bridges reach their theoretical strength value). However, the present analysis is conservative in the sense that we are considering the worst case where the tablet material behaves in a brittle fashion at all the length scales considered. To determine the failure stress of the monolithic material, the large difference in volume between the bridge, unit cell and any macroscopic specimen needs to be considered. With that in mind, we can review some of the most relevant results from the numerical analysis that can be put into the context of size effect and therefore evaluate the benefits of such microstructural design. Weibull statistics assumes the probability of survival for a specimen of volume V under stress σ as

$$P_s(\sigma) = \exp \left\{ -\frac{V}{V_b} \left(\frac{\sigma}{\sigma_f^T} \right)^k \right\} \quad (2)$$

where σ_f^T is the failure stress, V_b is the volume (e.g., of the bridge), and k is the Weibull parameter. The stress at which the monolithic specimen of volume V_m will survive with probability $1/e$ is then

$$\sigma^m = \left(-\frac{V_b}{V_m} \log P_s \right)^{1/k} \sigma_f^T = \left(\frac{V_b}{V_m} \right)^{1/k} \sigma_f^T. \quad (3)$$

Likewise, the strain energy of the monolithic material is defined as the energy dissipated by the solid until failure $U^m = (\sigma^m)^2/(2E^T)$. The Weibull modulus k for engineering ceramics is about 10, which is the value we will use for both Alumina and ABS.

For this analysis, the microstructure depicted in Fig. 4 is considered with both, ABS-chitosan and alumina-chitosan systems. The geometry and dimensions of the cases analyzed are those already described in Table 1. The results for this analysis are shown in Fig. 10(a) and (b) for the ABS-chitosan and Fig. 10(c) and (d) for the alumina-chitosan system. In particular, we focus our discussion for the case with $L_o/L = 0.4$ and $\theta = 1^\circ$ for both material systems, which is the geometry that gives the best energy dissipation without sacrificing too much of the composite's strength. The following discussion will address both, (i) the size effect of the tablet's strength and (ii) the size effect of the macroscopic material compared with the monolithic counterpart.

3.1. Tablet strength

One of the key microstructural features described in Section 2.1 is the mineral bridge. The mechanical properties, in particular the hardening behavior, strongly depend on the integrity of this important connection between the tablets. Indeed, the optimum energy dissipation is generally attained between tablet fracture and tablet pullout (see Fig. 11). We note in our results that the maximum principal stress, which is highest at the bridges, never reaches the strength of the material. In fact, the optimum case with $\theta = 1^\circ$ and $L_o/L = 0.4$ fails by hardening/tablet pullout on both materials' systems. Another important observation is that the principal stress in the rest of the tablet drops to less than half of its value at the bridge in most cases. For the particular case of alumina, the principal stress in the tablet remains below 100 MPa (being below 60 MPa in the $\theta = 1^\circ$ case). This indicates that the

tablets are far from experiencing brittle failure; even if we consider a possible reduction in strength due to the large difference in volume between the tablet and the bridge. For example, according to Eq. (3), if the strength of the alumina at the bridge is $\sigma_f^T = 350$ MPa (which has a volume $V_b = 0.005$ mm³ according to the dimensions given in Table 1), the strength of the unit cell or tablet (with volume $V_m = V_{\text{cell}} = 1.0\text{--}1.3$ mm³) falls to $\sigma_f^{\text{cell}} \approx 200$ MPa, which clearly demonstrates that the tablet in this geometry ($L_0/L = 0.4$ and $\theta = 1^\circ$) and length scale is not stressed to its limit.

The implications of such an analysis seem to suggest that the tablets and their bridges are not required to be stronger for this particular geometry and filler constitutive behavior. In other words, reducing the size of the unit cell (tablet and bridge size) to smaller scales (even nanoscale) to reach higher values of strength does not necessarily yield better energy dissipation, and flaw tolerance is indeed not required according to our results. Evidently, our model lends itself for optimization, and higher angles with higher tablet strength can be explored. In the case of alumina considered here (with $\sigma_f^T = 350$ MPa at the bridge), angles higher than 3° lead to tablet fracture which yield to lower values of energy dissipation. However, according to Eq. (3), reducing the size of the bridge from $b = 100$ to 10 μm , the tablet's strength would increase up to $\sigma_f^T = 470$ MPa making it possible for the tablets to pullout without fracture. The new results (different from those shown in Figs. 10(c), (d) and 11(c)) show an increase in the max energy dissipation (which then occurs at higher angles). The effect in increasing tablet angle and reducing the size of the bridge will ultimately reach a trade-off between failure at the bridge and failure at the dovetail of the tablet. We surmise that an absolute optimum will be achieved at the right combination of L_0/L and θ by which the artificial nacre maximizes its macroscopic strength and energy dissipation. One factor to keep in mind is that naturally occurring nacre does not exhibit waviness with angles higher than 5° .

Finally, we note that the values of the tensile strength for alumina at the bridge level considered in our analysis actually falls to very conservative values. It is known that typical strength of alumina is about 350 MPa. However, those values are typically obtained for macroscopic samples with dimensions above the mm size ($V = 1\text{--}1000$ mm³). Considering $\sigma_f^T = 350$ MPa at the bridge level means that the tablet material would yield more modest values of tensile strength if we were to test monolithic samples at macroscopic scales $\sigma_f = 100\text{--}200$ MPa.

3.2. Specimen size

In Section 2.5, it was shown that, once the optimal geometry is attained, the composite has the ability to spread damage avoiding localized failure, which means that artificial nacre retains its macroscopic response (e.g., strength and energy) independently of the specimen's size. That is, the strength of a macroscopic specimen is the same of the unit cell under homogeneous deformation. On the other hand, it is well known that a larger specimen of a monolithic material (like geological aragonite) tends to fail at a lower stress than a smaller specimen of the same material as the larger volume

contains more flaws. This important difference in behavior between the artificial nacre material and its monolithic counterpart is key to explain the benefits of making materials with these microstructures and therefore, size effects and appropriate material properties should be carefully discussed to enrich our previous analysis.

Assuming that the brittle material has a strength σ_f^T at size V_b , we compare side by side the strength and energy dissipation of two different specimens of the same volume V_m . The first specimen is completely made out of the monolithic brittle material which obeys Weibull statistics. This specimen will have a strength σ^m and an energy $U^m = (\sigma^m)^2/(2E^T)$ at size V_m obtained directly from Eq. (3) with $k = 10$. The second specimen is made of the artificial nacre studied in previous sections with strength σ^C and energy U^C . In the artificial nacre, the mineral phase only obeys Weibull statistics at the tablet and bridge levels (as previously discussed in Section 3.1). Once the dimensions of the tablet and bridge are fixed, the strength, σ^C , and energy, U^C , calculated at the unit cell will be that of the macroscopic material. Accordingly, σ^C/σ^m and U^C/U^m can be studied as a function of the specimen size to assess the benefits of the artificial nacre.

As previously shown, the artificial nacre with $L_0/L = 0.4$ and $\theta = 1^\circ$ fails in hardening/tablet pullout mode on both, alumina-chitosan and ABS-chitosan materials systems of interest. That means that any increase in material strength or, equally, any reduction in unit cell size does not change the results already shown in Section 2.5.1 (Fig. 10). We believe that it is reasonable to build master curves showing the strength and energy improvement trends for different V_m/V_b ratios as long as $V_b \leq 0.005$ mm³, with the maximum size given by the real bridge volume used in our previous calculations. It will be shown later on, that this is the bridge size for the artificial nacre specifically manufactured for this study. Any improvement or new processing techniques that can manufacture materials with smaller unit cells (and smaller bridges) will consequently follow the same failure mechanisms and therefore, the same master curves should be applicable. As such, Fig. 13 shows that σ^C/σ^m and U^C/U^m can be studied as a function of V_m/V_b for both material systems. It should be noted, that in our studies we use the bridge volume V_b as the reference volume at which the strength σ_f^T is defined. The unit cell with $L_0/L = 0.4$ and the dimensions specified in Table 1 will be regarded as the reference unit cell. For example, the results shown in Fig. 13 assume that the bridge strength is $\sigma_f^T = 350$ MPa for the alumina and $\sigma_f^T = 65$ MPa for the ABS for a bridge with volume $V_b = 0.005$ mm³.

In Fig. 13, two important results were included as a reference; (i) the results from naturally occurring nacre and (ii) the results obtained with $\theta = 0^\circ$. Both reference cases bring a significant perspective into this analysis. First, the results of the natural material are shown in terms of the σ^N/σ^m (indicated as Nacre Strength) and U^N/U^m as grey regions. One could take those values as the ultimate goal for material design and determine the necessary values of V_m/V_b (as long as the mineral's bridge size does not exceed its maximum V_b^{max}). In the alumina-chitosan case, modest values

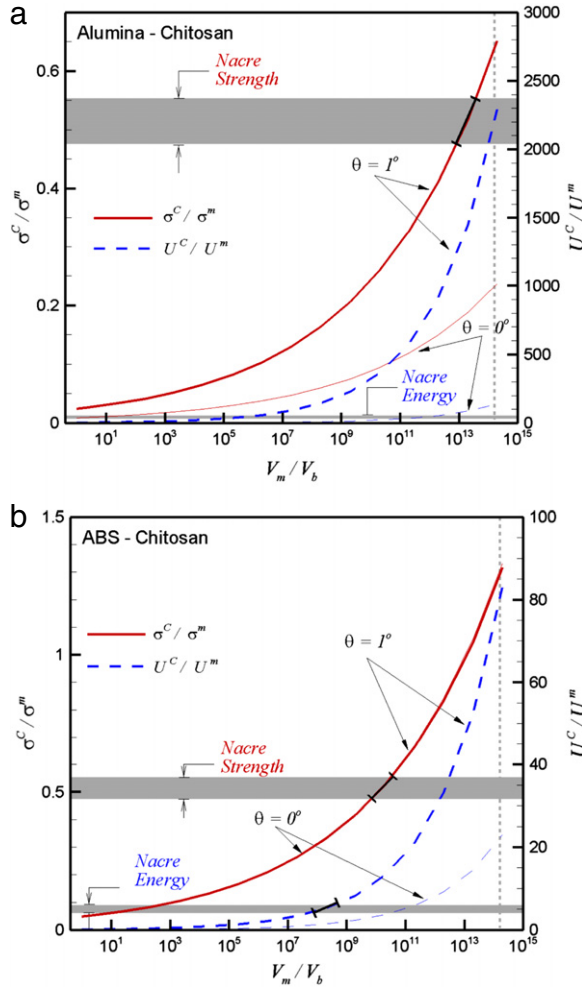


Fig. 13 – Size effects in terms of strength and energy. Assuming a geometry given by Table 1 and properties from Table 2 ($L_0/L = 0.4$ and $\theta = 1^\circ$), we then calculate the strength and therefore energy of a monolithic material at different sizes. (a) Size effect on alumina samples for $\sigma_f^T = 350$ MPa. (b) Size effect on ABS samples, $\sigma_f^T = 65$ MPa. As a reference we also include the comparison between the nacre vs. aragonite strength and energy, assuming a $V_m = 1 \text{ mm}^3$ sample, and the results with $\theta = 0^\circ$.

of $V_m/V_b \approx 2 \cdot 10^5$ can get a material with an energy improvement similar to those of Nacre (i.e., $U^N/U^m = 5.17\text{--}6.76$), but the σ^C/σ^m would barely reach 0.1. If the strength needs to be improved to similar values of those of nacre $\sigma^C/\sigma^m \approx 0.5$, one should consider volume $V_m/V_b \approx 2 \cdot 10^{13}$. Hence, artificial nacre made from this reference unit cell with the dimensions listed in Table 1, would exhibit nacre type improvement when compared to a monolithic specimen relatively large in size (e.g., a 5 m^3). However, the monolithic reference can be significantly reduced by reducing the unit cell with improved manufacturing techniques. This is not unreasonable if we consider that, for the case of naturally occurring nacre, the volume ratio is $V_m/V_b \approx 1.6 \cdot 10^{14}$ (which is basically considering a typical specimen size of monolithic material of the order of $V_m \approx 1 \text{ mm}^3$ and a nano-sized aragonite bridge of diameter and height of 20 nm).

It is also worth mentioning that for these volume sizes in alumina-chitosan, the improvement in energy is exceptionally larger than that of the naturally occurring nacre, which is $U^N/U^m \approx 1500$. These large values of energy improvement may seem excessive and not necessary (depending upon the targeted material properties). Therefore, from the viewpoint of obtaining the level of improvements achieved by the naturally occurring nacre, this seems to suggest that there is still room for improvement in our preliminary designs and that smaller values of V_m/V_b can eventually lead to a more optimum balance in σ^C/σ^m and U^C/U^m . Similar trends are found for the ABS-chitosan system (Fig. 13(b)). However the volume required to achieve similar levels of strength improvement with respect to the monolithic material is three orders of magnitude lower than that of the alumina-chitosan system (i.e. $V_m/V_b \approx 2 \cdot 10^{10}$).

The second set of reference curves included in the plots of Fig. 13 are the results of our calculations with $\theta = 0^\circ$. The significance of such comparison is to highlight the point that we want to emphasize in this work, which is the importance of the waviness and dovetail geometry in what otherwise is a plain brick-and-mortar structure that does not consider the mechanical interlocking and balance discussed in Section 2. Evidently, size effects, according to our simple Weibull model, are also shown to be beneficial even for flat tablets. However, this benefit is very limited in terms of the levels of improvement in strength and energy that one could obtain over those with dovetail geometries.

Evidently this analysis was carried out with a specific set of geometries and material systems. This particular case is limited in the sense that any change in the dovetail angle would not lead to any improvement in performance (lower angles lead to hardening-pullout failure and higher angles lead to bridge fracture both of which result in lower energy dissipation). Some other optimum configuration may be as well obtained if other material systems or size scales (different from those listed in Tables 1 and 2) are considered. In fact, we hypothesize that given sufficient strength in the tablets by, for instance reducing the size of the cell and tuning the relative volume between the tablet and bridges, higher stress levels could be reached at the tablets and therefore, take advantage of the strength at the local level as well. Along those lines, geometries with higher angle dovetails could be considered that eventually can lead to better improvements in strength and energy as discussed in Appendix A.1.

To illustrate this, let us consider the hypothetical case where the unit cell is reduced in size to the micron level. Considering a tablet with $L = 10\text{--}20 \text{ }\mu\text{m}$, keeping the same aspect ratio as those shown in Fig. 4 and Table 1, and the volume of the bridge to $V_b = 2.8 \cdot 10^{-10} \text{ mm}^3$, the strength would rise to $\sigma_f^T = 1850$ MPa (according to Eq. (3)). It should be noted that this unit cell size is not unrealistic if we take into account that current techniques can indeed lead to similar dimensions (Munch et al., 2008). Fig. 14 shows the normalized composite strength and energy dissipation with respect to the monolithic material for artificial nacre made of alumina and manufactured with these new dimensions. Like the previous case the overlap area is maintained as $L_0/L = 0.4$, however we vary the dovetail angle to $\theta = 0^\circ, 1^\circ$ and 5° . These results demonstrate two important points:

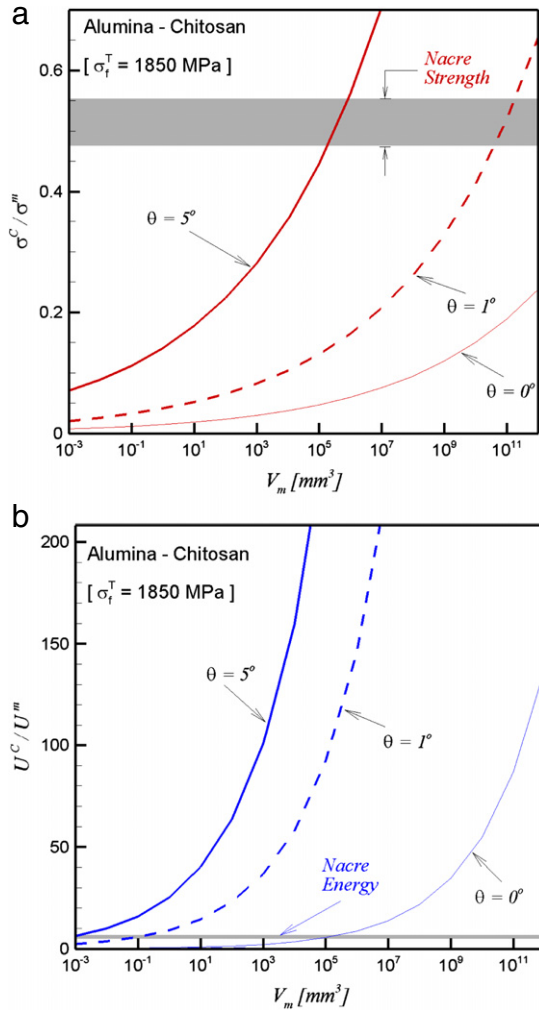


Fig. 14 – Size effects for the alumina-chitosan system when bridge size $V_b \approx 2.8 \cdot 10^{-10} \text{ mm}^3$ and $\sigma_f^T = 1850 \text{ MPa}$ for $\theta = 0^\circ, 1^\circ$ and 5° . (a) Normalized strength σ^C/σ^m and (b) Normalized energy dissipation U^C/U^m as a function of the macroscopic volume V_m .

(1) For angles $\theta = 0^\circ$ and 1° there is no real advantage in reducing the size of the unit cell (or otherwise, consider stronger bridges) with respect to the reference unit cell ($V_b = 0.005 \text{ mm}^3$). In fact, for $\theta = 1^\circ$, the volume required to achieve a level of improvement in strength on the order of $\sigma^C/\sigma^m \approx 0.5$ is still impractical as in the reference cases.

(2) Remarkably, the high strength of the bridges allow for better energy dissipation and strength at higher angles $\theta = 5^\circ$ (Fig. 18) achieving values of $\sigma^C/\sigma^m \approx 0.5$ at much smaller volumes for the monolithic counterpart, $V_m = 1 \cdot 10^5 \text{ mm}^3$. Again if specimens were built as cubes, each side would only be 5 cm long, which leads to more manageable specimens for lab testing and more practical components for a given application.

Evidently, this demonstrates the vast potential of these biomimetic materials. Firstly, the advantage of a composite material over that of the monolithic material is primarily manifested by the fact that, although the brittle tablet material and the macroscopic monolithic counterpart follow

a Weibull scaling law, the artificial nacre (once the size of its unit cell is fixed) is insensitive to size. That is, size effect only applies to the brittle tablet material. The well-established concept of the brick-and-mortar microstructure falls into this category. However, we showed that for these brick-and-mortar structures ($\theta = 0^\circ$) the improvement is very limited. This means that any increase in the tablet's strength does not yield improvements in the macroscopic material response. Second, in order to exploit the potential of these materials, one should not ignore the important contribution of the dovetail to the sliding mechanisms and the competition between tablet pullout and fracture. Therefore we can state that both, geometry and size are equally important and mutually linked. If one does not take into account the size scale, an optimum design will be limited by the strength of the bridge. Likewise, reducing the unit cell size and hence the size of bridges may not result in an improvement if one does not take into account the full load bearing capability of the bridges by allowing higher dovetail angles.

From the material design point of view, we should note that this work is only intended to pave the way to achieve better materials by showing some potential “blueprints” for biomimetic microstructures. We emphasize that there is clearly room for further exploration. By any means, this should not be considered as an exhaustive optimization work. A clear potential towards optimization is possible if one considers other material systems, stronger interfaces, different combinations of overlap/dovetail angles and, more importantly, other length scales. Such an optimization process would ultimately reach the point where higher angles begin to lead to fracture in the dovetail region, which may limit the capability of the bridges to withstand higher stresses. These limitations may guide us to a potential global optimum for material designs.

We surmise that naturally occurring nacre has been optimized so that $\sigma^N/\sigma^m = 0.54\text{--}0.61$, and $U^N/U^m = 5.17\text{--}6.76$ in a mm-sized specimen following these very same principles. Eventually, an optimization method that considers these complex systems and the various material failure mechanisms could lead to the right unit cell geometry and size required to achieve a targeted strength and energy dissipation. The challenges associated with such a task are related to the development of appropriate non-differentiable methods (associated with the nature of the objective function) and the development of reliable numerical techniques and physical models (such as the one we have presented here).

4. Experimental demonstration through rapid prototyping

To confirm the benefits of artificial nacre and the simulation predictions, rapid prototyped samples were made based on the previous dimensional analysis. Fused deposition modeling (FDM) is used to fabricate the samples (Stratasys FDM Titan USA). The brittle tablets are made of ABS while the polymer is a 50–50 wt% mixture of Dow Chemical Epoxies D.E.R. 331 and D.E.R. 732 with hardener D.E.H. 24. The material properties of both the ABS and Epoxy are listed in Table 6.

Table 6 – Material properties of ABS and Dow chemical epoxy. These values have been obtained from our own mechanical tests.

	E (MPa)	ν	σ_y (MPa)	σ_f (MPa)	ε_f^p (%)
ABS	1616	0.34	24	28.6	0.5
Epoxy	451	0.48	1.75	9.94	16.3

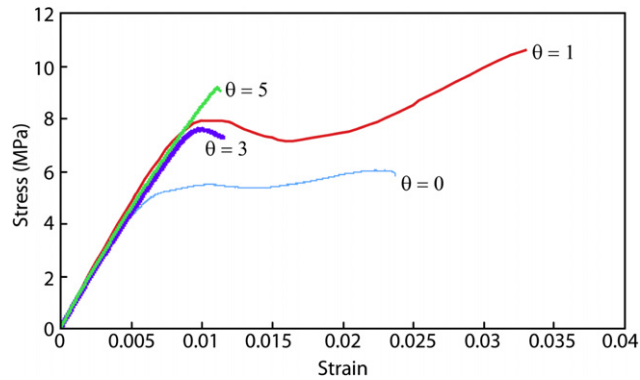


Fig. 15 – ABS-epoxy system with $L_o/L = 0.678$: Stress-strain response as a function of dovetail angle. Blue curve corresponds to $\theta = 0^\circ$, red to $\theta = 1^\circ$, purple to $\theta = 3^\circ$ and green to $\theta = 5^\circ$. (For interpretation of the references to colour in this figure legend, the reader is referred to the web version of this article.)

Tensile samples were created based on the geometry seen in Fig. 4(a). The dimension here are $b = 0.3$ mm, $h = 0.3$ mm, and $L_t = 12$ mm (total length of the unit cell). A similar parametric study was conducted varying θ and L_o . In this experimental study, θ varied between 0° and 5° , while L_o varied between 2.4 mm (short dovetail overlap) and 6 mm (long dovetail overlap). From testing these samples, we find a design with the best performance, which material response corresponds to that seen in the previous dimensional analysis as well as naturally occurring nacre.

4.1. Experimental stress-strain curves

We tested the samples in tension using an MTS Syntec 20/G tensile testing machine with a constant strain rate of 0.02 mm/min. First we tested the samples with a long dovetail overlap and varied θ (Fig. 15). From this graph the effect of θ is apparent and we can see that a dovetail angle of 1° gives the best response (red dashed line). The 1° sample results in the highest stress and strain to failure. We also see softening after the initial peak stress, followed by hardening due to interlocking of the tablets during sliding. Note that the 1° sample presents a very similar response to that of Fig. 7(a) ABS1. The same initial softening followed by hardening due to the locking effect of the dovetail is observed. Approximately 30 samples in total were tested. The trends are similar for each respective sample (i.e., for each θ and L_o value), thus showing consistency during testing.

For all tested samples, we see the departure from linear elasticity at higher stresses as θ increases. When $\theta = 0$ the lowest yield stress, followed by minimal strain hardening and

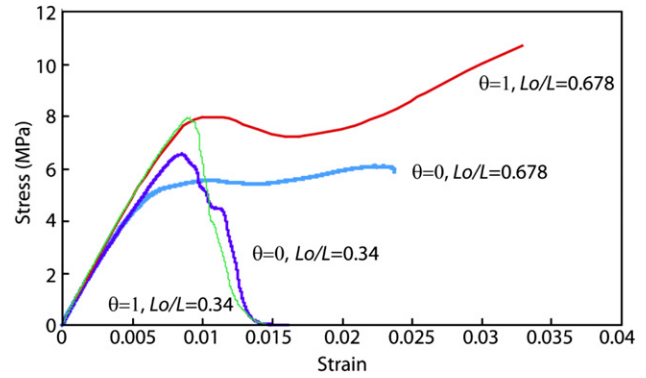


Fig. 16 – ABS-epoxy system: Stress-strain response for varying overlaps length and θ .

failure at a strain of $\sim 2.5\%$ is observed. At $\theta = 5^\circ$, the material yields at the highest measured yield stress followed by brittle tablet failure. For the investigated ABS-epoxy system, we can conclude that as θ increases, the yield stress increases, but that as θ goes beyond 1° , brittle failure ensues. This failure response again proves that the 1° sample is optimal. The 0° sample exhibits a ductile behavior but less deformation upon failure due to localization. The 1° sample exhibit a greater failure strain due to its damage spreading capabilities.

We also investigated the effect of θ on varying overlap lengths. Fig. 16 shows the material response of a short dovetail overlap length with $\theta = 0^\circ$ and 1° , and a long overlap length with $\theta = 0^\circ$ and 1° . The measured stress-strain responses illustrate the effect of dovetail overlap length with respect to dovetail angle. We see that the peak stresses for $\theta = 0^\circ$ and $\theta = 1^\circ$ are relatively the same. However, with the short dovetail overlap length, softening and pullout after the initial peak stress were observed, whereas with a longer dovetail overlap length, hardening and greater strain to failure were measured. In agreement with the numerical simulations, these results show that a sufficient dovetail overlap length is necessary for hardening and large strains to develop. The above experimental results from this chart support the trends seen in Fig. 7(b) where the transition from the first curve to the second occurs during a period of larger stress due to a larger overlap length. We directly see this trend between a shorter and longer dovetail overlap length again supporting the previously reported dimensional analysis.

Finally, we note that the material properties of the filler are different from those of the chitosan used in our numerical predictions. However, even if the chitosan Young's Modulus is four times greater than the one used in our experiments, our experimental results show remarkable similarities with those curves shown in Fig. 7. Differences in the absolute values of the strength and energy only reflect the predicted variations of interface properties. In our experiments we notice that the ABS/epoxy interfaces are much stronger than our simulated interfaces. Indeed, our numerical studies on the effect of interface strength effectively predict a strong coupling between macroscopic composite strength and cohesive maximum traction (or strength). On the other side, our artificial nacre closely resembles the stiff tablet/soft interface nacre model as the Young's Modulus of the epoxy is smaller than that of the ABS tablets.

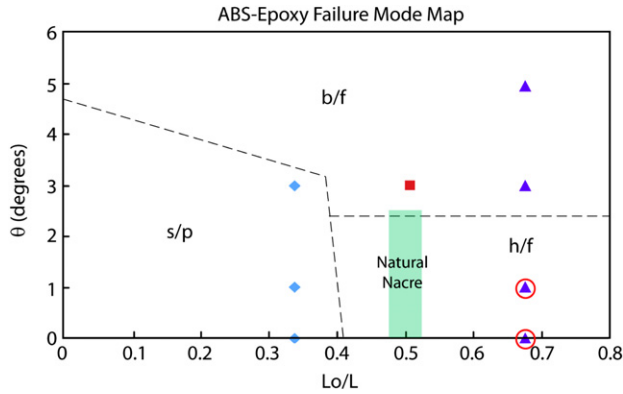


Fig. 17 – ABS-epoxy system: Failure mode map for all tested samples. Data points circled in red have the highest energy dissipation. As a reference, values of L_0/L and θ correspond to the microstructure of nacre are also plotted. (For interpretation of the references to colour in this figure legend, the reader is referred to the web version of this article.)

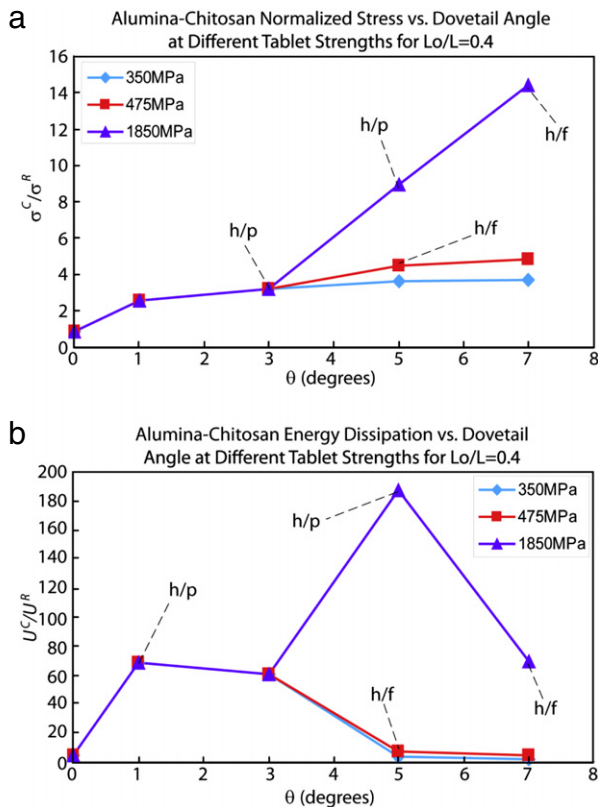


Fig. 18 – (a) Normalized strength as a function of dovetail angle for different tablet strengths and a constant $L_0/L = 0.4$. (b) Energy dissipation as a function of dovetail angle for different tablet strengths at a constant $L_0/L = 0.4$. For both graphs, the failure modes are shown. (For interpretation of the references to colour in this figure legend, the reader is referred to the web version of this article.)

Table 7 – Energy dissipation results where U^C is the total energy of the composite sample and U^R is the energy at yield of the zero degree sample (dashed line in schematic of Fig. 9).

L_0/L	Dovetail angle (deg)	U^C/U^R	U^C/U^R (ABS-Chit)
0.68	0	5.16	4.22
0.68	1	12.69	10.69
0.68	3	2.43	6.64
0.68	5	2.52	4.87
0.51	3	2.87	6.59
0.34	0	2.30	3.54
0.34	1	2.46	12.43
0.34	3	2.29	7.05

4.2. Energy dissipation of experimental samples

To further quantify gains resulting from the tested artificial nacre, normalized energy was calculated for each sample in the same fashion as Section 2.5. Here we normalize the total energy of the composite by the energy at yield of the composite sample with a zero degree dovetail angle (for the artificial material this reference value, U^R is 0.0223 mJ/m^3). Yielding of the sample with zero degree dovetail angle corresponds to the onset of the epoxy yielding. We do this by calculating the energy under the stress strain curve at a 0.2% offset (dashed area in Fig. 9). Table 7 lists the calculated results for the normalized energy. We note that the 1° sample (in bold) with a long dovetail overlap exhibits a two-fold increase in normalized energy when compared to the other samples. In this analysis, it is important to note that, based on our material constraints with rapid prototyping, the filler material is not optimized. Thus, the filler material can be optimized for a given tablet material so that the yield stress of the filler is close to the yield stress of the tablet (similar to the material parameters used in the computations). Nevertheless, we measured an increase in energy dissipation in our best sample, which is similar to natural nacre; however, an optimized filler material could produce further energy dissipation.

4.3. Transitions between characteristic behaviors: experiments

In order to parallel the findings reported in Fig. 11, we created a failure map of all the tested samples. Using the same normalized overlap length, L_0/L and dovetail angle, we show in Fig. 17 the modes of failure identified in each sample. For a short dovetail overlap length we identified softening and pullout. However, as the overlap length increased, the dovetail angle had a larger impact on the failure mode. Samples with a dovetail angle of 0° and 1° experienced hardening and fracture, while samples with a dovetail angle of 3° or greater failed in a brittle manner (b/f notation in Fig. 17). From Barthelat et al. (2007) we obtained a range of L_0/L and θ as measured in natural nacre. We can see from this chart that the failure mode of natural nacre corresponds to that of our optimal 1° sample. Also we see that our optimal sample corresponds to the optimal ABS-chitosan sample from the simulations.

5. Concluding remarks

In this work, we address the need for a systematic study and analysis of the design parameters of artificial nacre, which is necessary to fully understand the interplay between microstructural and material properties. A general methodology is presented to identify failure modes and conduct a parametric analysis in dimensionless space, which is particularly suitable to the design of optimized bioinspired materials.

A design for artificial nacre that incorporates the critical features of nacre is investigated, and a systematic numerical analysis of a subset of the design parameter space is carried out. It is shown that in order to replicate the deformation mechanisms of nacre, a delicate balance must be struck between the morphology of the structure and the properties of the constituent materials. As expected, the resulting composite is weaker than the monolithic cell made of tablet material but for some morphologies it exhibits significantly higher energy dissipation (resilience).

The uniaxial stress–strain response of the proposed artificial nacre design exhibits stress softening/hardening, and failure through tablet fracture/tablet pullout. In this work we show that the transitions between these characteristic responses are dictated by a complex interplay of several parameters in the design space. Furthermore, the numerical analysis reveals the physical mechanisms behind these transitions as the geometry and material properties are varied. For instance, we demonstrated that the relative values of $E^F J / T_{\max}^2 L$ and T_{\max} / σ_f^T act synergistically to dictate the behavior of the system and lead to maximum energy dissipation. Likewise, certain optimized combinations of θ and tablet overlap length result in peaks in the dissipation energy.

We then proceeded to analyze the significance of size effect following simple size scaling rules. As opposed to previous works (Gao et al., 2003), we did not use the concept of flaw tolerance and theoretical strength. Instead, we assumed that the material can contain defects at all length scales, be brittle/flaw sensitive and consequently follow simple scaling laws such as those described by Weibull statistics. Such scaling laws have been successfully applied to brittle materials (Bazant and Chen, 1997) even for small scale structures and devices (Peng et al., 2006). First, our analysis suggests that significant improvements can already be achieved by “segmenting” the material to prevent the specimen strength from being size dependent. This rule simply implies that, once the size of the building block (e.g., tablet) is fixed, the strength of the unit cell remains constant regardless of the size of the specimen. The implication of such a rule first predicts a modest improvement in strength and energy with respect to a monolithic specimen, with a simple brick-and-mortar configuration. However, the benefit is clearly demonstrated for those microstructures that contain dovetail (wavy) geometries. Evidently, optimization of these geometries requires knowledge of the material strength at the bridge and tablet level.

Along the same lines, we confirmed that the desired macroscopic strength and energy dissipation is then attained

by controlling the geometry and size scale together. However, size scale controls the strength of the tablet's material up to a certain point. Evidently the scaling laws we used predict an increase in the tensile strength by decreasing the volume of the bridge. For instance, this is useful to allow larger L_0/L and/or θ . At a given point, the bridge becomes so strong that dangerous levels of stress may build up at the dovetail features of the tablets. At that point, further reduction in tablet size would result in failure mode change. Once a certain geometry and necessary tablet/bridge tensile strength is achieved, any further increase in strength does not result in better performance. This may explain why nacre does not need the tablet to be extremely strong as claimed in Gao et al. (2003). We surmise that an optimum configuration will be one that finds a good balance between avoiding fracture at the bridge vs. fracture at the tablet and maximizing tablet sliding up to complete tablet pullout. Hence, the optimum configuration is one that dissipates the most energy through tablet sliding without fracture.

We were also able to manufacture prototypes based on the findings from the numerical model and conduct a similar parametric study. Through this we varied the dovetail overlap length and θ to identify performance gains. The best design corresponded to the greatest energy dissipation, which corresponded to a hardening up to failure. Similar to those observed in the simulations, our experiments also exhibited distinct failure modes, softening with tablet pullout, hardening followed by fracture, and brittle failure. Furthermore we were able to show that the failure modes of natural nacre and the simulated ABS-chitosan system leading to maximum energy dissipation, are the same as that of our best design.

The performance metric defined in terms of strength and resilience (toughness) of the composite means that the desired behavior is that of stress hardening and failure by tablet pullout. Although the complexity of the transitions makes it difficult to formulate an explicit relationship between the values of the parameters and the resulting stress–strain response, the insights into the mechanisms and the broad trends of the response to variations in the parameters imply that the most relevant parameter space is much reduced. Nonetheless, optimal design requires a more extensive sampling of the design space, which is computationally very expensive. This points at the need of using optimization schemes with advanced sampling algorithms and identification of surrogate models capable of interpolating and extrapolating the FEM data.

In general, our results appear to imply that a precise control on the geometry of some key microstructural features is essential for optimum synthetic material performance. In fact, our results show sensitivity of the optimum dissipation energy, with significant changes in strength and energy dissipation for relatively small variations in the angle. However, our proposed model still does not consider stochastic factors that may allow some of these geometrical constraints to be more flexible in an average sense. The current model considers that all the microstructural features depicted in Fig. 4 repeat periodically over the entire composite material. This is a strong constraint arising from the computational cost. However, more advanced computational

models should be considered to study the effect of randomness on the most important geometrical parameter and local material properties (such as bridge size, tablet overlap or even mineral strength). Naturally occurring nacre is a good example in this sense. From the manufacturing point of view, these observations are very important considering that some process induced imperfections can be allowed, making the potential processing of these materials possible.

The full impact of this work emerges in the context of new material systems and processing techniques being developed to control the fine scale geometry of microstructures as well as the chemical composition of its constituents and interfaces. Many of these new methodologies are now showing signs of progress and researchers in the realm of material science and chemistry are beginning to seek design guidelines from the mechanics community. For instance, techniques such as layer-by-layer (LBL) assembly (Bonderer et al., 2008; He et al., 1997; Kato, 2000; Podsiadlo et al., 2007a,b; Tang et al., 2003; Wei et al., 2007), ice templation (Deville et al., 2006; Munch et al., 2008), thin film deposition (Chen et al., 2007a), and self-assembly (Heuer et al., 1992; Sellinger et al., 1998; Zhang et al., 2006), have been developed. For a review, see Espinosa et al. (2009). These techniques have shown to lack, or have limited ability to control, the waviness and other morphological features (e.g. bridges) of the tablets, constituent volume fraction, aspect ratios, and the close-packed formation and high conformity of tablets as observed in natural nacre. In this sense, materials produced with these techniques have some morphological resemblance to nacre but do not replicate it mechanistically. On the other hand, new techniques based on mineralization, with particle size and shape control through in-situ biomineralization and scaffold processing are currently emerging with the promise to better control the abovementioned microstructural features. Therefore, it is likely that small scale synthetic materials mimicking nacre not only morphologically but also mechanistically will be attained in the next decade.

Acknowledgements

HDE acknowledges the support of General Motors Company through contract No. TCS10643, ARO through MURI Award No. W911NF-08-1-0541 and ONR through Awards N00014-08-1-0108, N00014-07-1-1139, and N00014-08-1-1055.

Appendix

A.1. Effect of tablet and bridge tensile strength

While in the previous section we used the parameters set forth in Table 2, we now wish to evaluate the effect of tablet tensile strength. By increasing the tablet's strength to 475 MPa and then 1850 MPa, we observe a remarkable increase in energy dissipation and normalized strength as the dovetail angle increases. Fig. 18 shows this effect for a constant normalized overlap length of $L_0/L = 0.4$. It is

also worth noting that the optimum angle for maximum energy dissipation shifts to higher values. This increase in energy and shift in optimum angle can be explained by the transition between the failure mechanisms at higher angles: at lower tablet strengths, the dominating failure mechanism is hardening/fracture whereas at higher tablet strengths, it is hardening/pullout. This can be easily appreciated for $\theta = 5^\circ$ where the energy dissipation increases almost two orders of magnitude when the tablet strength is 1850 MPa (Fig. 18).

While this analysis shows a clear trend, that increasing the tablet's strength allows us to design tablets with higher angles achieving higher energy dissipation and strength, we anticipate that this behavior will presumably reach an optimum as higher stresses will start developing at the rest of the tablet due to the stress concentrations in the dovetail region of the tablets at higher angles. That is, as the dovetail increases, and stress concentration in the rest of tablet (not in the bridge) becomes significantly more prominent. Another failure mechanisms triggered by the fracture of the tablet at the dovetail region may limit the amount of energy dissipation that one can get out of high angle designs.

Fig. 18 also shows that tablet strength has no effect on the strength and energy for low angles ($\theta \leq 3^\circ$). This is due to the fact that a tablet strength of 350 MPa is already high enough to withstand the maximum principal stress developed at the bridges. All these observations have important connotations in terms of the lessons learned from nacre: first, at lower angles, the strength of the tablet (beyond a certain value) does not have any effect on the macroscopic response of the composite material. This means that the tablets do not need to be extremely strong (e.g., with tensile strength close to their theoretical values). However, on the other side, in order to take advantage of the tablet's strength, one can optimize the angle to achieve the maximum energy dissipation without significantly sacrificing strength. To add another dimension to this problem, we argue that tablet strength, for a given tablet material, can also be improved by considering size effects (Section 3). Therefore, we surmise that nature not only optimized material combination and shape, but also the length scale of its building blocks.

A.2. Effect of cohesive parameters

The dimensionless parameters for the cohesive interfaces are the relative maximum traction T_{\max}/σ_f^T , and the relative fracture length scale $E^F J/T_{\max}^2 L$. Since the stiffness of the cohesive elements K is not varied, it is clear from Fig. 5 that the effect of increasing J at a given T_{\max} is to slow the rate of element degradation. The effect of these varying parameters on the macroscopic tensile behavior on the ABS-chitosan and alumina-chitosan systems is shown in Fig. 19. Both σ_f^C/σ_f^R and U^C/U^R increase with increasing $E^F J/T_{\max}^2 L$ and T_{\max}/σ_f^T . In particular, both σ_f^C/σ_f^R and U^C/U^R reach saturation with $E^F J/T_{\max}^2 L$. It should also be mentioned that for the highest values of T_{\max} and $E^F J/T_{\max}^2 L$, the values of the maximum displacement in the cohesive law are relatively large compared to the overlap region.

In the ABS-chitosan system the value of T_{\max}/σ_f^T is varied from 7.7×10^{-3} to 7.7×10^{-2} , a 10-fold increase, and

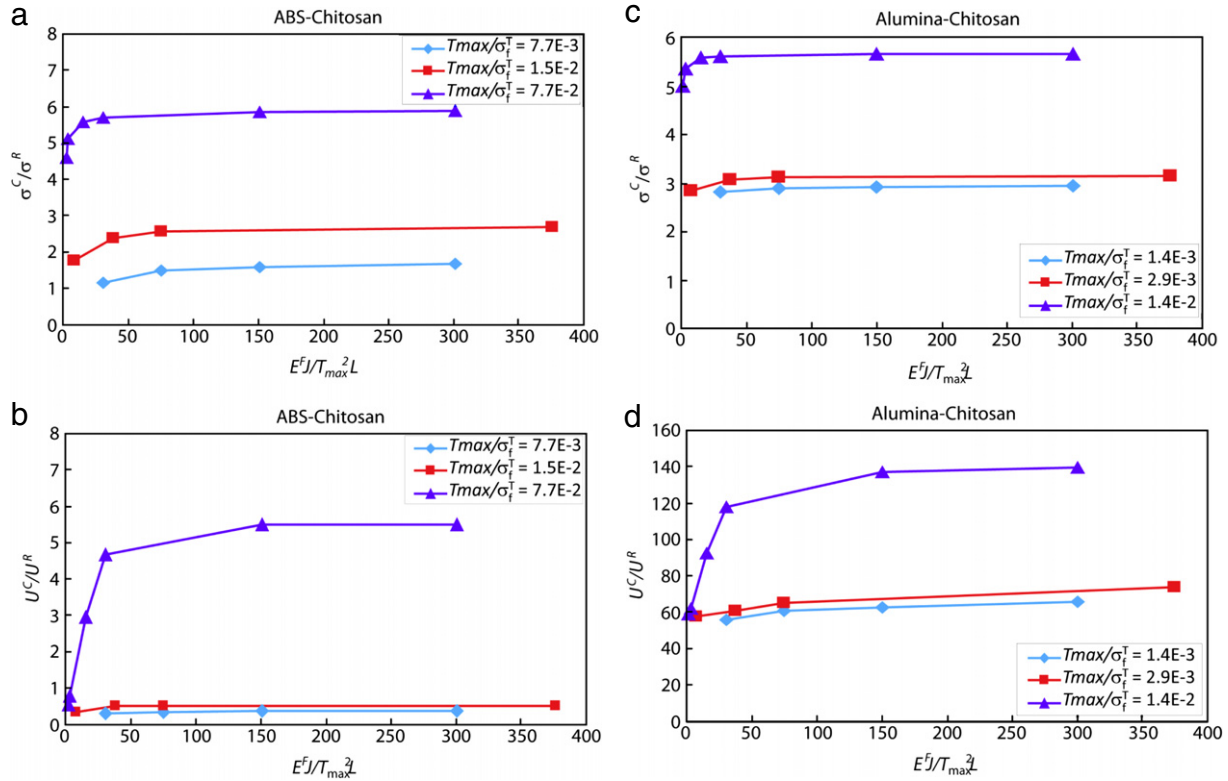


Fig. 19 – (a) σ_f^C / σ_f^T and (b) U^C / U^R of the ABS-chitosan system as a function of $E^f J / T_{max}^2 L$ for T_{max} / σ_f^T values of 7.7×10^{-3} , 1.5×10^{-2} , and 7.7×10^{-2} ; (c) σ_f^C / σ_f^T and (d) U^C / U^R of the alumina-chitosan system as a function of $E^f J / T_{max}^2 L$ for T_{max} / σ_f^T values of 1.4×10^{-3} , 2.9×10^{-2} , and 1.4×10^{-2} . The failure modes for the ABS-chitosan composite are stress hardening and tablet fracture for $T_{max} / \sigma_f^T = 7.7 \times 10^{-3}$ and 1.5×10^{-2} and stress hardening and tablet pullout for $T_{max} / \sigma_f^T = 7.7 \times 10^{-2}$. The alumina-chitosan composite fails through stress hardening and tablet pullout. (For interpretation of the references to colour in this figure legend, the reader is referred to the web version of this article.)

$E^f J / T_{max}^2 L$ is increased up to 3×10^3 . The uniaxial normalized stress-strain curves of the ABS-chitosan composite with $T_{max} / \sigma_f^T = 7.7 \times 10^{-3}$ and increasing $E^f J / T_{max}^2 L$ are plotted in Fig. 20(a). The strains at which the tablet fractures are marked with a red circle. Since T_{max} and the stiffness of the cohesive law K are the same, the initial elastic regime where the cohesive elements are still intact is not affected by increasing $E^f J / T_{max}^2 L$. Once the cohesive elements reach T_{max} , the rate of degradation is slower for larger $E^f J / T_{max}^2 L$. At small $E^f J / T_{max}^2 L$, the fast degradation and failure of the cohesive elements cause the temporary dip in stress. As $E^f J / T_{max}^2 L$ is increased, the slow rate at which the cohesive elements fail means that the average stress continues to increase. Note that once $E^f J / T_{max}^2 L$ reaches a point where the cohesive elements are able to retain their adhesion up to the stress state at which hardening (due to the dovetails) prevails, the effect of $E^f J / T_{max}^2 L$ on the overall stress of the composite becomes negligible. This causes σ_f^C / σ_f^T and U^C / U^R to saturate. With a stronger interface of $T_{max} / \sigma_f^T = 7.7 \times 10^{-2}$, the composite transitions to stress hardening/tablet pullout, with a commensurate large increase in U^C / U^R to achieve the desirable increase in toughness, $U^C / U^R > 1$. Thus the relative values of the parameters $E^f J / T_{max}^2 L$ and T_{max} / σ_f^T act together to dictate the behavior of the system.

For the alumina-chitosan system, the value of T_{max} / σ_f^T is increased from 1.4×10^{-3} to 1.4×10^{-2} . The failure mode for all values of $E^f J / T_{max}^2 L$ and T_{max} / σ_f^T examined is tablet pullout, with $U^C / U^R > 1$. The dependence of σ_f^C / σ_f^T and U^C / U^R on T_{max} / σ_f^T and $E^f J / T_{max}^2 L$ displays similar trends, and can be also understood in the same way. Fig. 20(b) is a plot of the normalized stress-strain curves of the alumina-chitosan composite with $T_{max} / \sigma_f^T = 1.4 \times 10^{-2}$ and increasing $E^f J / T_{max}^2 L$. Again, the initial linear regime where the cohesive elements possess their full stiffness is unaffected; once the interface starts to degrade, the slower rate of degradation acts to increase the stress, thereby raising the values of both σ_f^C / σ_f^T and U^C / U^R . While σ_f^C / σ_f^T values are relatively similar for both systems, U^C / U^R values for the alumina-chitosan system are an order of magnitude larger.

A.3. Effect of bridge thickness

As mentioned previously, tablet fracture always occurs in the bridge in our simulations. This makes the normalized bridge dimension b/L an important parameter to consider. As previously discussed by Barthelat et al. (2007) the

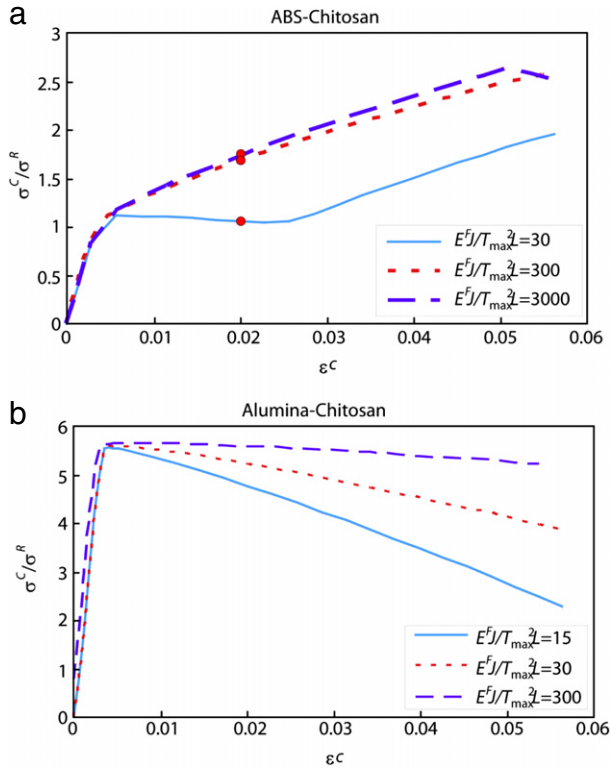


Fig. 20 – The normalized stress–strain curve of (a) ABS-chitosan composite for $T_{max}/\sigma_f^T = 7.7 \times 10^{-3}$ and (b) alumina-chitosan composite for $T_{max}/\sigma_f^T = 1.4 \times 10^{-2}$, for different values of $E^f/T_{max}^2 L$.

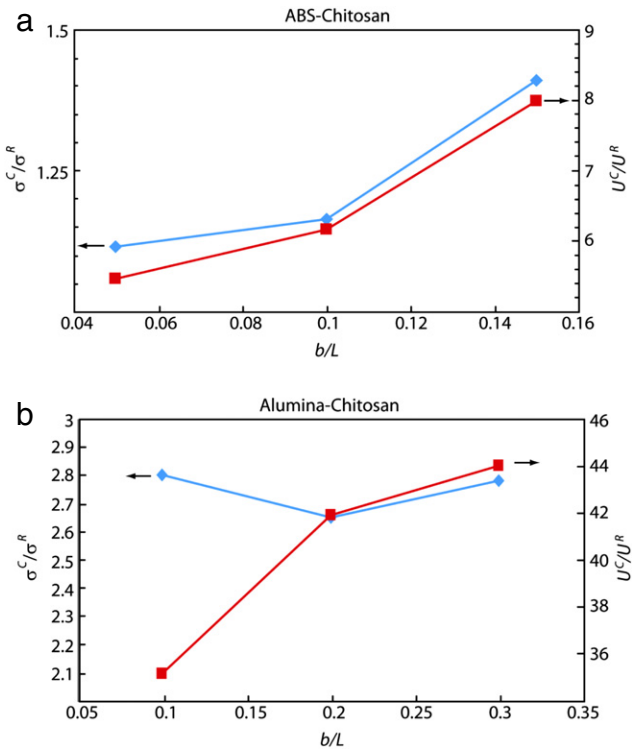


Fig. 21 – σ_f^C/σ_f^R and U^C/U^R as a function of b/L for the (a) ABS-chitosan and (b) alumina-chitosan composites.

combination of tension and compression in the core and overlap area, respectively, is one of the key mechanisms to increase energy dissipation by tablet sliding. Resistance to tablet sliding is mainly driven by the dovetail angle in the overlap area, which induces lateral expansion (Fig. 2(b)). The role of the bridges is to provide lateral constraint in the core area to equilibrate this lateral expansion and therefore indirectly offering resistance to tablet sliding. The capability of the tablets to remain connected by these bridges strongly depends on the tablet's strength and their geometry (i.e., bridge thickness). The effect of the strength was previously discussed in Appendix A.1. We will now discuss the effect of the bridge thickness.

Although it seems straightforward to expect that a thicker bridge will lead to stronger composite and thus larger values of σ_f^C/σ_f^R and U^C/U^R , the results point to a more complex picture. σ_f^C/σ_f^R and U^C/U^R are plotted for the ABS-chitosan and aluminum-chitosan systems in Fig. 21. For the ABS-chitosan composite, the failure mode at the data points is stress hardening and tablet fracture. In this case, the results are as expected: the fracture of the tablet is delayed when the bridge is thicker which leads to increases in both σ_f^C/σ_f^R and U^C/U^R . For the alumina-chitosan composite σ_f^C/σ_f^R decreases as b/L is increased while U^C/U^R always increases. This is because the failure mode for the composite at these data points is stress hardening and tablet pullout. Tablet pullout means that the maximum principal stress $\max_{\text{tablet}} \sigma_1^T$ is smaller than the strength of the tablet through the course of the simulation. In this case, a larger bridge dimensions lowers the maximum principal stress in the bridge even further but the change in thickness is still small and does not significantly affect the overall stress–strain relation of the composite. The optimal bridge dimension is therefore a function of the material parameters and the mode of failure. The normalized dissipated energy, U^C/U^R , increases monotonically but saturates at high values of b/L .

REFERENCES

- Ballarini, R., Kayacan, R., Ulm, F.J., Belytschko, T., Heuer, A.H., 2005. Biological structures mitigate catastrophic fracture through various strategies. *International Journal of Fracture* 135, 187–197.
- Barthelat, F., Espinosa, H.D., 2007. An experimental investigation of deformation and fracture of nacre-mother of pearl. *Experimental Mechanics* 47, 311–324.
- Barthelat, F., Li, C.M., Comi, C., Espinosa, H.D., 2006. Mechanical properties of nacre constituents and their impact on mechanical performance. *Journal of Materials Research* 21, 1977–1986.
- Barthelat, F., Rim, J.E., Espinosa, H.D., 2009. A review on the structure and mechanical properties of mollusc shells—perspectives on synthetic biomimetic materials. In: Bhushan, B., Fuchs, H. (Eds.), *Applied Scanning Probe Methods XIII Biomimetics and Industrial Applications*. Springer.
- Barthelat, F., Tang, H., Zavattieri, P.D., Li, C.M., Espinosa, H.D., 2007. On the mechanics of mother-of-pearl: a key feature in the material hierarchical structure. *Journal of the Mechanics and Physics of Solids* 55, 306–337.
- Bazant, Z.P., Chen, E.P., 1997. Scaling of structural failure. *Applied Mechanics Reviews* 50.

- Bonderer, L.J., Studart, A.R., Gauckler, L.J., 2008. Bioinspired design and assembly of platelet reinforced polymer films. *Science* 319, 1069–1073.
- Chen, L., Ballarini, R., Kahn, H., Heuer, A.H., 2007a. A bioinspired micro-composite structure. *Journal of Materials Research* 22, 124–131.
- Chen, L., Ballarini, R., Kahn, H., Heuer, A.H., 2007b. Bioinspired micro-composite structure. *Journal of Materials Research* 22, 124–131.
- Currey, J.D., 1977. Mechanical properties of mother of pearl in tension. *Proceedings of the Royal Society of London* 196, 443–463.
- Deville, S., Saiz, E., Nalla, R.K., Tomsia, A.P., 2006. Freezing as a path to build complex composites. *Science* 311, 515–518.
- Espinosa, H.D., Barthelat, F., 2007. “Segmented layered composite with dovetail shaped tablets” inclusions: ‘nacre’ composite. NU Disclosure No. 26164, USA.
- Espinosa, H.D., Rim, J.E., Barthelat, F., Buehler, M.J., 2009. Merger of structure and material in nacre and bone—perspectives on de novo biomimetic materials. *Progress in Materials Science* 54, 1059–1100.
- Evans, A.G., Suo, Z., Wang, R.Z., Aksay, I.A., He, M.Y., Hutchinson, J.W., 2001. Model for the robust mechanical behavior of nacre. *Journal of Materials Research* 16, 2475–2484.
- Gao, H.J., Ji, B.H., Jager, I.L., Arzt, E., Fratzl, P., 2003. Materials become insensitive to flaws at nanoscale: lessons from nature. *Proceedings of the National Academy of Sciences of the United States of America* 100, 5597–5600.
2010. Granta CES Edupack Material Selection Software.
- He, J.L., Li, W.Z., Li, H.D., 1997. Simulation of nacre with TiN/Pt multilayers and a study of their hardness. *Journal of Materials Research* 12, 3140–3145.
- Heuer, A.H., Fink, D.J., Laraia, V.J., Arias, J.L., Calvert, P.D., Kendall, K., Messing, G.L., Blackwell, J., Rieke, P.C., Thompson, D.H., Wheeler, A.P., Veis, A., Caplan, A.I., 1992. Innovative materials processing strategies—a biomimetic approach. *Science* 255, 1098–1105.
- Jackson, A.P., Vincent, J.F.V., Turner, R.M., 1988. The mechanical design of nacre. *Proceedings of the Royal Society of London* 234, 415–440.
- Ji, B.H., Gao, H.J., 2004. Mechanical properties of nanostructure of biological materials. *Journal of the Mechanics and Physics of Solids* 52, 1963–1990.
- Kato, T., 2000. Polymer/calcium carbonate layered thin-film composites. *Advanced Materials* 12, 1543–1546.
- Kotha, S.P., Li, Y., Guzelsu, N., 2001. Micromechanical model of nacre tested in tension. *Journal of Materials Science* 36, 2001–2007.
- Li, X.D., Xu, Z.H., Wang, R.Z., 2006. In situ observation of nanograin rotation and deformation in nacre. *Nano Letters* 6, 2301–2304.
- Mayer, G., 2005. Rigid biological systems as models for synthetic composites. *Science* 310, 1144–1147.
- Mayer, G., 2006. New classes of tough composite materials—lessons from natural rigid biological systems. *Materials Science & Engineering C: Biomimetic and Supramolecular Systems* 26, 1261–1268.
- Munch, E., Launey, M., Alsem, D., Saiz, E., Tomsia, A., Ritchie, R., 2008. Tough, bio-inspired hybrid materials. *Science* 322, 1516–1520.
- Ortiz, C., Boyce, M., 2008. Materials science: bioinspired structural materials. *Science* 319, 1053–1054.
- Peng, B., Espinosa, H.D., Moldovan, N., Xiao, X., Auciello, O., Carlisle, J.A., 2006. Fracture size effect in UNCD—applicability of Weibull theory. *Journal of Materials Research*.
- Podsiadlo, P., Kaushik, A.K., Arruda, E.M., Waas, A.M., Shim, B.S., Xu, J.D., Nandivada, H., Pumplin, B.G., Lahann, J., Ramamoorthy, A., Kotov, N.A., 2007a. Ultrastrong and stiff layered polymer nanocomposites. *Science* 318, 80–83.
- Podsiadlo, P., Liu, Z.Q., Paterson, D., Messersmith, P.B., Kotov, N.A., 2007b. Fusion of seashell nacre and marine bioadhesive analogs: high-strength nanocomposite by layer-by-layer assembly of clay and L-3,4-dihydroxyphenylalanine polymer. *Advanced Materials* 19, 949–955.
- Pugno, N., 2006. Mimicking nacre with super-nanotubes for producing optimized super-composites. *Nanotechnology* 17, 5480–5484.
- Ruoff, R., Pugno, N., 2005. Strength of nanostructures. Do materials become insensitive to flaws at nanoscale?: An answer based on quantized fracture mechanics and nanoscale Weibull statistics. In: *Mechanics of the 21st Century*. pp. 303–311.
- Sarikaya M, Aksay IA (Eds.), 1995. *Biomimetics, Design and Processing of Materials*, Woodbury, NY.
- Schaeffer, T.E., IonescuZanetti, C., Proksch, R., Fritz, M., Walters, D.A., Almqvist, N., Zaremba, C.M., Belcher, A.M., Smith, B.L., Stucky, G.D., Morse, D.E., Hansma, P.K., 1997. Does abalone nacre form by heteroepitaxial nucleation or by growth through mineral bridges? *Chemistry of Materials* 9, 1731–1740.
- Sellinger, A., Weiss, P.M., Nguyen, A., Lu, Y.F., Assink, R.A., Gong, W.L., Brinker, C.J., 1998. Continuous self-assembly of organic-inorganic nanocomposite coatings that mimic nacre. *Nature* 394, 256–260.
- Smith, B.L., Schaeffer, T.E., Viani, M., Thompson, J.B., Frederick, N.A., Kindt, J., Belcher, A., Stucky, G.D., Morse, D.E., Hansma, P.K., 1999. Molecular mechanistic origin of the toughness of natural adhesives, fibres and composites. *Nature (London)* 399, 761–763.
- Tang, H., Barthelat, F., Espinosa, H.D., 2007. An elasto-viscoplastic interface model for investigating the constitutive behavior of nacre. *Journal of the Mechanics and Physics of Solids* 55, 1410–1438.
- Tang, Z.Y., Kotov, N.A., Magonov, S., Ozturk, B., 2003. Nanostructured artificial nacre. *Nature Materials* 2, 413–418.
- Wang, R.Z., Suo, Z., Evans, A.G., Yao, N., Aksay, I.A., 2001. Deformation mechanisms in nacre. *Journal of Materials Research* 16, 2485–2493.
- Wei, H., Ma, N., Shi, F., Wang, Z.Q., Zhang, X., 2007. Artificial nacre by alternating preparation of layer-by-layer polymer films and CaCO₃ strata. *Chemistry of Materials* 19, 1974–1978.
- Weibull, W., 1951. A statistical distribution function of wide applicability. *ASME Journal of Applied Mechanics* 18, 293–297.
- Zhang, X., Liu, C.L., Wu, W.J., Wang, J.F., 2006. Evaporation-induced self-assembly of organic-inorganic ordered nanocomposite thin films that mimic nacre. *Materials Letters* 60, 2086–2089.